



**Arab American University**

**Faculty of Graduate Studies**

**Enhancement of Electrical Performance of MoO<sub>3</sub> Films  
via Indium Nano Sandwiching**

**By**

**Masa Jamal Daraghmeh**

**Supervisor**

**Dr. Muayad Abu Saa**

**Co supervisor**

**Dr. Hazem Khanfar**

**This thesis was submitted in partial fulfillment of the  
requirements for the Master's degree in Physics**

**December/2018**

**© Arab American University – 2018.**

**All rights reserved.**

**Enhancement of Electrical Performance of MoO<sub>3</sub> Films via Indium Nano Sandwiching**

**By**

**Masa Jamal Daraghmeh**

This thesis was defended successfully on December- 8- 2018 and approved by:

Committee members

Signature

1- Dr. Muayad Abu Saa/ Supervisor

.....

2- Dr. Hazem Khanfar/ Co Supervisor

.....

3- Prof. Dr. Atef Fayez Qasrawi/ internal Examiner

.....

4- Prof. Mohammad saed / External Examiner

.....

## **Declaration**

The work provided in this thesis, unless otherwise referenced, is the researcher's own work, and has not been submitted elsewhere for any other degree or qualification.

Student's Name: Masa Jamal Daraghmeh

Signature:

Date: December-8- 2018

**Declaration**

**To My Parents**

## Acknowledgment

First and foremost, I praise God, the almighty for giving me this chance and granting me the capability for its success. This current form of my thesis is due to the guidance and helping of many people. So I would like to offer my thanks to all of them.

I start with my dear mother, who was the first to support me and to encourage me to get the master's degree. She followed me step by step in all my successes and difficulties. All the wonderful words in the world are not enough to express my great gratitude. And I will not forget my Father, who will encourage me in every step in all my studies. Let me steal a line to whom the characters will not be able to reward him, made my ambition a coordinated way seeing it in their eyes. My husband be confident that this line will not be sufficient for you.

I respect and thank Prof. Dr. Atef Qasrawi, for giving me all support and guidance which made me complete the thesis duly. I am extremely thankful to him for providing such a nice support and guidance, although he had busy schedule managing the laboratory affairs. I owe my deep gratitude to my thesis supervisors Dr. Muayad Abu Saa and Dr. Hazem Khanfar, who took keen interest on my thesis work and guided me all along, till the completion of my thesis work by providing all the necessary information for developing a good thesis. I would not forget to remember all the doctors Department of Physics Prof. Dr. Zaki Saleh, Dr. Adli Saleh, Dr. Ahmad Omar, Prof. Mohammad Abu Samra, Dr. Soliman Rabaa, and Mr. Anan Hussien, for their encouragement and more over support. I have greatly profited from the courses I took, the high quality knowledge I reserved and all opportunities that I had when I worked as a teaching and assistant. Special thanks to Prof- Mohammed Al-Saeed to complete

my thesis duly. I have no words in my dictionary to express my thanks to my brothers and sisters. Ahmad, Ayham, Adham, Sewar and Eman for their constant support. They were one of the first friendly faces to greet me when I began this master's thesis. Special thanks for my best friends, especial Olfat Omareya, Fatima abu alrub and Hadil aloushi for the special years we had spent together.

I present my thesis gift to my dear daughter Mesk.

# **Enhancement of Electrical Performance of MoO<sub>3</sub> Films via Indium Nano Sandwiching**

**By**

**Masa Jamal Daraghmeh**

**Supervisor**

**Dr. Muayad Abu Saa**

**Co supervisor**

**Dr. Hazem Khanfar**

## **Abstract**

In this thesis the impact of the Indium nanolayers on the characteristics of MoO<sub>3</sub> thin films are explored. Indium metallic nano- layers of thicknesses of 50, 75, 100 and 200 nm are sandwiched between two 500 nm thick MoO<sub>3</sub> thin films. The X-ray diffraction technique is used to find out the structural properties of the MoO<sub>3</sub> and MoO<sub>3</sub>/In/MoO<sub>3</sub> layers. In accordance with this technique, MoO<sub>3</sub> exhibit crystalline form called orthorhombic structure  $\alpha$ -MoO<sub>3</sub> phase. The indium induced formation of crystalline phase when its thickness exceeds 50 nm. In addition, the impact of the indium thickness on the electrical performance of the films was searched in a wide range of temperature. It was observed that the dielectrical conductivity is highly sensitive to temperature and indium thickness. Electrically almost no difference was observed between the hall bar and van der pauw type samples. Both conduct by thermionic emission revealing an activation energy that become deeper with increased indium thickness. Furthermore, the room temperature frequency dependent impedance, conductance and capacitance were measured in the frequency range of 10-1800 MHz. Remarkable shift in the frequency value of maximum conductance was observed upon

indium layer enhancement. The theoretical analysis and computer simulations that targeted the exploration of the physics of resonance phenomena which is accompanied with by negative capacitance phenomena have shown that, the Au/MoO<sub>3</sub>/C device is of tunneling diode type in which the current conduction covert from tunneling to correlated barrier hoping at 300 MHz. This type of study is expected to open the doors for efficiently utilize the MoO<sub>3</sub> films in optoelectronic technology with less resistance and best optoelectronic achievement.

## List of contents

Title	Page No.
List of tables	xi
List of figures	xii
Chapter One	Introduction and Literature Survey
	1
Chapter Two	Theoretical Background
	4
2.1	The X – ray diffraction
	4
2.1.1	Bragg’s law
	4
2.1.2	The formula to calculating the lattice constant of types structures
	6
2.1.3	Derivation of scherrer equation
	6
2.2	Electrical Characteristics
	10
2.2.1	Van der Pauw’s Theorem
	11
2.2.2	Hall bar technique
	13
2.3	Impedance Spectroscopy
	14
2.3.1	AC Capacitance
	15
2.3.2	The reflection coefficient
	18
2.3.3	The return loss
	18
Chapter Three	Experimental Details
	19
3.1	Preparation of samples.
	19
3.2	The geometrical shape and optical image nanosandwiching films
	21
3.3	X- ray diffraction (XRD) measurements
	23
3.4	The Impedance measurements
	26
3.5	The electrical measurements
	27

	3.6	The "hot-probe" technique	30
Chapter Four		Results and discussion	31
	4.1	Structural analysis	31
	4.1.1	Samples deposit as grown onto glass	31
	4.1.2	Samples deposit as grown onto Au substrate.	35
	4.2	Electrical Characteristics	40
	4.2.1	I-V response of van der pauw and Hall bar samples as grown	41
	4.2.2	Comparison between van der pauw and hall bar technique to calculate the conductivity.	44
	4.2.3	Effect of indium on electrical conductivity	46
	4.2.4	Temperature dependent conductivity	46
	4.3	Impedance Spectroscopy	52
Chapter Five		Conclusions	61
References			63
المخلص			70

---

**List of tables**

---

No.	Title	Page No.
4.1	Mechanical parameters for MIM-75 nm, MIM-100 nm and MIM-200 nm.	33
4.2	Mechanical parameters for $\alpha$ -MoO <sub>3</sub> and Au for Au/MIM-200 nm	38
4.3	Lattice mismatch for all samples	39
4.4	The conductivity for all samples MIM at room temperature.	43
4.5	The activation energy for samples.	49
4.6	The fitting parameter of capacitance model for Au/MIM/C samples.	55

---

## List of figures

No	Caption	Page No.
2.1	Schematic stretching of Bragg's law which can be derived from the triangle ABC.	5
2.2	X-ray diffraction by a crystal with thickness $t$ and diffraction curve for the crystal.	8
2.3	The geometry of van der pauw method	11
2.4	Graph of Van Der Pauw function	13
2.5	Hall- bar geometry	14
3.1	The physical vapor deposition system. a. from inside. b. from outside	20
3.2	The geometrical design of MIM and Au/MIM thin films.	22
3.3	Appearance of the sandwiched films $d=0, 50, 75, 100$ and $200\text{nm}$	22
3.4	The geometrical design of Au/MIM/Au thin films	22
3.5	Rikagu Miniflex 600 diffractometer	23
3.6	Schematic view of Bragg-Brentano system	25
3.7	Agilent 4291B 1.0 M-1.8 GHz impedance analyzer	26
3.8	Electrical measurement setup	28
3.9	The hall bar designed	29
3.10	The van der Paw designed	29
3.11	Experimental set-up of the "hot-probe" experiment	30
4.1	XRD pattern of indium metal and the (MIM) sandwiched films as grown (Measured at room temperature).	32
4.2	XRD pattern of Indium (In), gold (Au) metals and the (Au/MIM) sandwiched films as grown measured at room temperature.	36
4.3	I-V response of van der pauw MIM ( $75$ and $100\text{nm}$ ) as grown at room temperature	41

4.4	I-V response of Hall bar MIM all samples as grown at room temperature.	42
4.5	Conductivity of van der pauw and Hall bar of all samples MIM.	44
4.6	The conductivity of Hall bar for all samples $\delta$ Vs T (K).	46
4.7	Conductivity of Hall bar for all samples $\text{Ln}(\delta)$ Vs T (K).	47
4.8	Conductivity of Hall bar for all samples $\text{Ln}(\delta)$ Vs $1000/T$ (K) <sup>-1</sup> .	48
4.9	Activation energy of Hall bar for all samples	50
4.10	The results of the AC signal analysis for the capacitance of Au/MIM/C in the frequency range of 0.01 GHz -1.8 GHz.	52
4.11	The capacitance spectra for the Au/MIM-0, 50, 75, 200 nm/C devices, where the pink line is the experiment data and the blue the modeling data using Equ. (2.29).	53
4.12	The conductance spectra in the frequency range of (0.01 GHz - 1.8 GHz) for Au/MIM-0nm/C, Au/MIM-50nm/C, Au/MIM-75nm/C, Au/MIM-100nm/C, Au/MIM-200nm/C sandwiched films	56
4.13	The impedance spectral for Au/MIM/C with frequency from zero to 1.8 GHz	57
4.14	The reflection coefficient for Au/MIM/C with frequency from zero to 1.8 GHz	58
4.15	The return loss for the Au/MIM/C as a function of frequency in the range of 1.0 MHz-1.8 GHz	59

---

## Chapter One

### Introduction and Literature Survey

Field of molybdenum oxide ( $\text{MoO}_3$ ) thin films is one of most active research areas.  $\text{MoO}_3$  materials are attractive among the transition-metal oxides due to their unusual chemistry produced by the multiple valence states. They can be used in a wide variety of applications such as cathodes in rechargeable batteries, superconductors, thermoelectric materials, field emission and electrochromic devices [1-6]. In addition, the molybdenum oxide crystal films may be used as solar cells [7]. Moreover,  $\text{MoO}_3$  finds application as a cathode material in the development of high energy density solid-state micro batteries, imaging devices, gas sensors [8], supported catalysts and lubricants [9].  $\text{MoO}_3$  have a great artistic significance because of to their electronic properties. These materials can be applied in other enforcement such as solid state microbatteries. The substoichiometric film  $\text{MoO}_3$  with oxygen lack contain surplus metal atoms which work as doping centers, these centers control the electrical film Characteristics [10].

The growth of  $\text{MoO}_3$  films is done by different deposition methods including the thermal evaporation, electron beam evaporation, sputtering, electrodeposition, sol-gel process, and chemical vapor deposition [11-14]. Lin et al prepared  $\text{MoO}_3$  films by sol-gel process heated at  $360^\circ\text{C}$ . At this temperature, the phase transformation from the amorphous to the crystalline  $\text{MoO}_3$  film occurs [15]. Moreover, the experimental results of Yang et al showed that thickness and heat-treatment temperature will have the string influence on the electrochromic properties of  $\text{MoO}_3$  thin films [8]. Furthermore, thin films of  $\text{MoO}_3$  were attended by spray

pyrolysis method on glass substrates, by using 0.1 M of molybdenum, effect of substrate temperature on the structural properties range from 200 to 300 C, the films are made in the range from 250 to 300° C are polycrystalline with orthorhombic symmetry and the films which prepared at 200° C are monoclinic. The orthorhombic status ( $\alpha$ -MoO<sub>3</sub>) has a layered structure. MoO<sub>3</sub> thin films are prepared by various routes, such as flash evaporation [10].

In another work of Kamoun et al, an aqueous solution of ammonium Molybdate including different condensation of Europium (0–2%) is sprinkled on a glass substrate heated at 460 °C in air, X-ray diffraction (XRD) turns out that all the generated films crystallized in the form of Orthorhombic  $\alpha$ -MoO<sub>3</sub> [16], Orthorhombic molybdenum trioxide ( $\alpha$ -MoO<sub>3</sub>) nanorods have been industrialized widely using a hydrothermal technique for electrochemical energy storage supercapacitor devices [17]. Kalantar-Zadeh et al, described the MoO<sub>3</sub> plates of Nano scale thickness, they are wrought from various basic plates of orthorhombic  $\alpha$ -MoO<sub>3</sub>, these plates are made of double layers of the deformed MoO<sub>6</sub> octahedra, which can be processed in bulk and at low cost synthesis road that combines mechanical exfoliation and thermal evaporation. The minimum resolvable thickness of these plates is 1.4 nm which is equal to the thickness of two double-layers inside one unit cell of the  $\alpha$ - MoO<sub>3</sub> crystal, as measured by the Atomic force microscopy (AFM) [18].

Due to their special physical and chemical properties, MoO<sub>3</sub> have many applications in electronic devices, the conductivity values of MoO<sub>3</sub> ranges from dielectric MoO<sub>3</sub> to semiconductor Mo<sub>18</sub>O<sub>52</sub> ( $\rho = 78.1 \Omega \cdot \text{cm}$ ) [19]. In another experiment, which carried out on MoO<sub>3</sub> powders calcined at different temperatures using a system operating under high vacuum conditions demonstrated that the dc-conductivity increases by more than five orders of magnitude with an increase in the working temperature from 77–300 K. These results also

revealed a high dependence of dc-conductivity on the calcination temperature for the  $\text{MoO}_3$  products. The presence of at least three different electrical conduction mechanisms for the same  $\text{MoO}_3$  tablet is revealed by the dependence of dc-conductivity on the operating temperature [20]. The threshold switching in thin-film metal-oxide-metal (MOM) structures with Mo oxides provides the possibility of this material to be applicable in oxide electronics as micro- and nanostructured switching elements [21].

In this thesis the  $\text{MoO}_3$  films was reshaped during the nanosandwiching technique. This technique is based on entering nanometallic (Indium) layers of thickness between 50 nm to 200 nm in the structure of  $\text{MoO}_3$  films. The indium sandwiching between two layers of  $\text{MoO}_3$  films are probably to change the physical characteristic of  $\text{MoO}_3$ . Thus the structural, electrical and impedance characteristic of the sandwiched films will be studied in order to explore the features and applications of this structure.

In the second chapter, all the basic theories used in the thesis was discussed, such as debating the Bragg's law and the Sherrer equation and anticipating the practical results needed to analyze the results.

In the third chapter, the measurements that are taken by our devices in the lab will be discussed. The evaporation process will be discussed for thin films, XRD for study structure, electrical and impedance, all of which will be presented in details.

In chapter four, we present our results in detail, discussing the structural characteristics in detail and the electrical properties obtained through the experiments and study other results in details. The conclusions will be discussed in chapter five.

## Chapter 2

### Theoretical background

#### 2.1 The x-ray diffraction.

X-ray Diffraction (XRD) is innovated for enforcement in the microstructure mensuration and in-depth research realization. XRD is a diffraction system in several domains so the X-ray diffractometry (XRD) that are significant for the description of materials, X-ray diffractometer supply the structure analysis of polycrystalline, single crystal and amorphous materials. The X-ray scattering methods are gropes of non-destructive analytical methods which display properties about the crystalline structure, thin films and physical features of materials, these methods depend on watching the scattered intensity of an X-ray beam hitting a sample as a function of incident, polarization, scattered angle and wavelength, where the characteristics and functions of materials relate on the crystal structures, therefore X-ray diffraction properties have been on a range wide applied as means in materials research, production and development so that XRD is an indispensable method for materials characterization [22].

##### 2.1.1 Bragg's Law.

The principle known as the Bragg's law is based on constructive interference of monochromatic X-ray radiations, where the constructive interference shows if it was the path of the partial waves on the lattice planes, when the beam collides with the atoms at a certain level  $hkl$  a constructive intervention happened when the difference in path length is an integer number of wavelengths as shown in Fig.2.1 [23].

Constructive interference occurs only when:

$$n\lambda = CB + CD \quad (2.1)$$

Where  $CB = CD$  ;

$$CB = d\sin\theta \quad (2.2)$$

$$n\lambda = 2d\sin\theta \quad (2.3)$$

Where ( $\lambda$ ) is the wavelength of the incident wave, ( $d$ ) is the lattice inter planar spacing of the crystal, ( $n$ ) is a positive integer and ( $\theta$ ) is the angle of incidence [24].

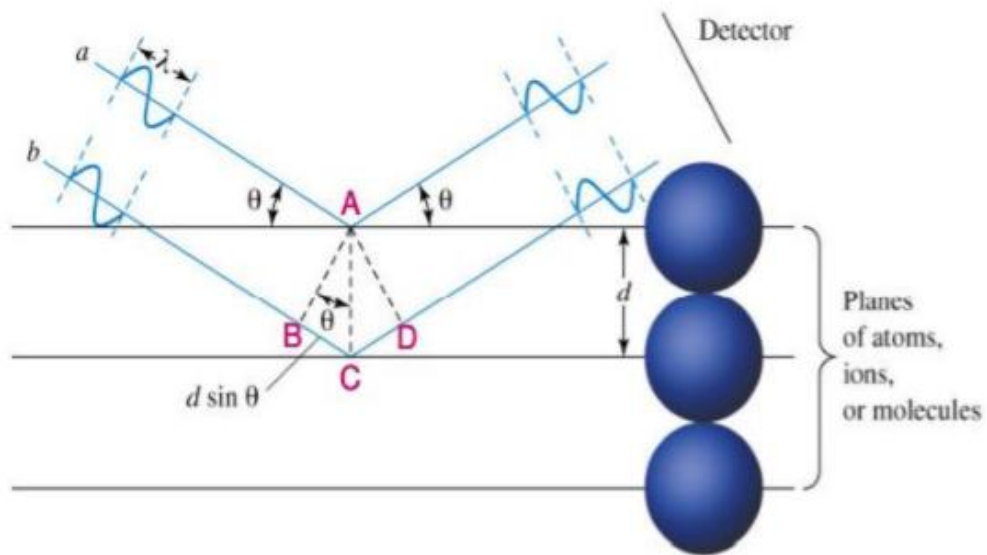


Figure 2.1: Schematic stretching of Bragg's law which can be derived from the triangle ABC [25].

### 2.1.2. The formula to calculating the lattice constant of types structures.

The relation between  $d$  and the lattice constant for type's structures is expressed mathematically by:

Tetragonal structure is:

$$\frac{1}{d_{hkl}^2} = \left( h^2 + k^2 + l^2 \left( \frac{a}{c} \right)^2 \right) \left( \frac{1}{a^2} \right) \quad (2.4)$$

Cubic structure is:

$$\frac{1}{d_{hkl}^2} = (h^2 + k^2 + l^2) \left( \frac{1}{a^2} \right) \quad (2.5)$$

Orthorhombic structure is:

$$\frac{1}{d_{hkl}^2} = \frac{h^2}{a^2} + \frac{k^2}{b^2} + \frac{l^2}{c^2} \quad (2.6)$$

Where,

$a$ ,  $b$  and  $c$  are the lattice constants.

$h$ ,  $k$  and  $l$  are miller indices.

### 2.1.3 Derivation of scherrer equation.

Scherrer equation is determine the crystallite size ( $D$ ). In 1918, Scherrer was suggested a formula that linked between the width of the X-ray diffraction peak and the crystallite size ( $D$ ). The scherrer equation is given as:

$$D = \frac{K \lambda}{\beta \cos \theta} \quad (2.7)$$

Where,  $\beta$  is the peak expanding at full width half maximum peak , the constant  $K$  is the form factor which associated to crystallite form and normally taken 0.94,  $\lambda = 0.15418$  nm is the x-ray wavelength and  $\theta$  is the Bragg angle [26]. The easier method to derivative the scherrer equation is the differentiation of Bragg's law, let  $n=1$  and multiplying both side of equation (2.3) by an integer  $m$ , then the equation becomes:

$$m\lambda = 2 m d \sin(\theta) \quad (2.8)$$

Since that the interplanar distance  $d$  doubled with  $m$  integers equal the thickness of crystal ( $t$ ), then the equation (2.8) simplifies as:

$$m\lambda = 2 t \sin(\theta) \quad (2.9)$$

This equation can also be explained as the  $m^{\text{th}}$  order reflection from a group of planes with an interplanar distance ( $t$ ). By differentiate both side of equation (2.9) and observed that  $m\lambda$  is constant, this yields to:

$$0 = 2 \Delta t \sin(\theta) + 2 t \cos \theta \Delta\theta \quad (2.10)$$

$$t = \frac{\Delta t \sin(\theta)}{\cos(\theta) \Delta\theta} \quad (2.11)$$

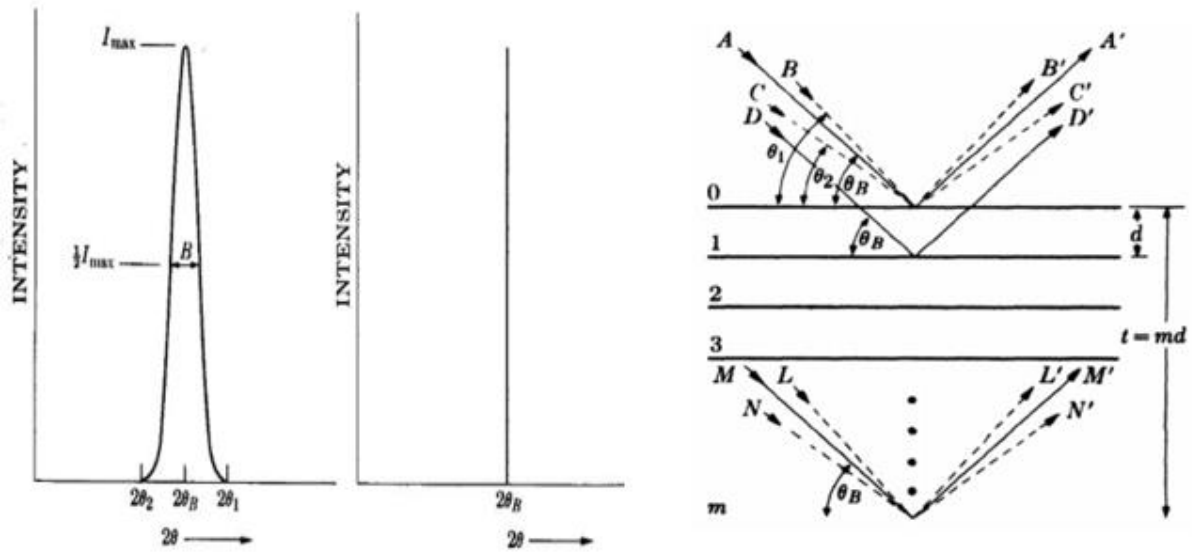


Figure 2.2: X-ray diffraction by a crystal with thickness  $t$  and diffraction curve for the crystal [27].

Since the small increment in the thickness is  $d$  ( $\Delta t = d$ ),  $d \sin(\theta) = \lambda/2$  from equation (2.3), and  $\Delta\theta$  can be positive or negative, so the absolute value must be taken.  $\Delta\theta$  is the half width of the peak and ( $2\Delta\theta = \beta$ ) is the full width half maximum peak. The substituting of these factors in equation (2.11) gives:

$$t = \frac{d \sin(\theta)}{\cos(\theta) \Delta\theta} = \frac{\lambda}{2 \cos(\theta) \Delta\theta} \quad (2.12)$$

$$t = D = \frac{\lambda}{\cos(\theta) \beta} \quad (2.13)$$

If the Gaussian function is applied to represent the peak, a shape factor  $K = 0.94$  is applied.

Then Scherrer equation will be given as [27]:

$$D = \frac{0.94 \lambda}{\cos(\theta) \beta} \quad (2.14)$$

In addition, the stacking faults (SF), micro-strains ( $\varepsilon$ ) and dislocation densities ( $\delta$ ) defined by the following relations. The differences of the micro strain ( $\varepsilon$ ), which arises from displacement of the unit cells about their normal positions.

$$\text{micro - strain } (\varepsilon) = \frac{\beta}{4 \tan \theta} \quad (2.15)$$

The dislocation density ( $\delta$ ) is an irregular atom distribution within a crystal structure, it is the total length of dislocation lines per unit area:

$$\delta = \frac{15\varepsilon}{aD} \quad (2.16)$$

Where ( $a$ ) is the lattice constant.

A stacking fault ( $SF$ ) is a kind of defect which characterizes the disordering of crystallographic planes. It is thus considered a planar defect. It is any defect that alters the periodic sequence of layers, these defects may be a wrong layer inserted into the sequence, a change of the layer sequence or a different translation between two subsequent layers, the stacking faults ( $SF$ ) can be calculated as equation [28]:

$$SF = \frac{2\pi^2\beta}{45\sqrt{3}\tan\theta} \quad (2.17)$$

We calculate the lattice mismatch between the MoO<sub>3</sub>, Indium and Au layers by using the equation [29]:

$$\Delta_1 = \frac{a_{MoO_3} - a_{In}}{a_{In}} \times 100\% \quad (2.18)$$

$$\Delta_2 = \frac{a_{MoO_3} - a_{In}}{a_{MoO_3}} \times 100\% \quad (2.19)$$

$$\Delta_3 = \frac{a_{MoO_3} - a_{Au}}{a_{MoO_3}} \times 100\% \quad (2.20)$$

Where the lattice mismatches causes dislocation at the surface and it related to the maximum allowed epitaxial layer. In the equation,  $a_{MoO_3}$ ,  $a_{In}$  and  $a_{Au}$  is the lattice constant of MoO<sub>3</sub>, indium and Au, respectively.

## 2.2 Electrical Characteristics.

The activity of electrons in the solid determines its electrical properties, but the task of obtaining the actual behavior of the electron in crystalline matter is a difficult task, there are many electrons interact with each other and with the atoms that constitute the lattice structure.

Until the electrical conduction occurs, electrons must have more energy than the energy gap to control and overcome the energy barrier. Depending on the extent of the energy gap for each material, it is classified as insulator, semiconductor or conductor. Conductors have their valence band and conduction band overlapped so they have free electrons moving in all parts of the material, but the insulators have a wide band gap which stops electrons movement, semiconductors contains a small band gap so many electrons can hop to the conduction band when the material is affected by an electric field [30].

The electrical conductivity of a semiconductor is related to the temperature by [31]:

$$\sigma = \sigma_0 \exp\left(-\frac{Ea}{kT}\right) \quad (2.21)$$

Where ( $\sigma_0$ ) is the pre-exponential factor, ( $Ea$ ) is the activation energy, ( $T$ ) is the temperature in kelvin and ( $k$ ) is Boltzmann constant.

Thus,

$$\ln\sigma = \ln\sigma_0 - \frac{Ea}{kT} \quad (2.22)$$

### 2.2.1 Van der Pauw's Theorem.

Van der pauw is a method to determine the resistivity of sample as shown Fig 2.3.

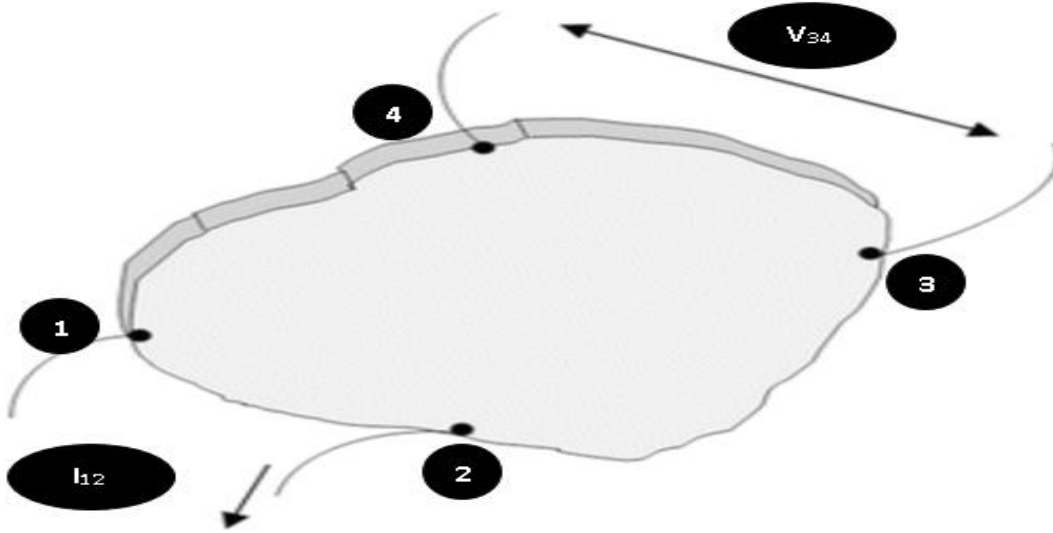


Figure. 2.3: The geometry of van der pauw method [32].

$$R_{12,34} = \frac{V_{34}}{I_{12}} \quad (2.23)$$

Where, ( $V_{34}$ ) is the voltage connected between points 3 and 4 and ( $I_{12}$ ) is the current connected between points 1 and 2.

To calculate the resistivity for van der pauw sample:

$$\rho = \frac{\pi t(R_1 + R_2)}{2 \ln 2} f\left(\frac{R_1}{R_2}\right) \quad (2.24)$$

Where;

$$R_1 = \frac{V_{23}}{I_{14}} \quad (2.25)$$

( $V_{23}$ ) is the voltage connected between points 2 and 3 and ( $I_{14}$ ) is the current connected between points 1 and 4.

And,

$$R_2 = \frac{V_{34}}{I_{12}} \quad (2.26)$$

Where  $\left( f\left(\frac{R_1}{R_2}\right) \right)$  is known Van der Pauw function (function of ratio of the potential difference  $V_{23}$  and  $V_{14}$ ). The Van der Pauw function displayed in figure 2.4. When the contacts are symmetrical the function should equal one.

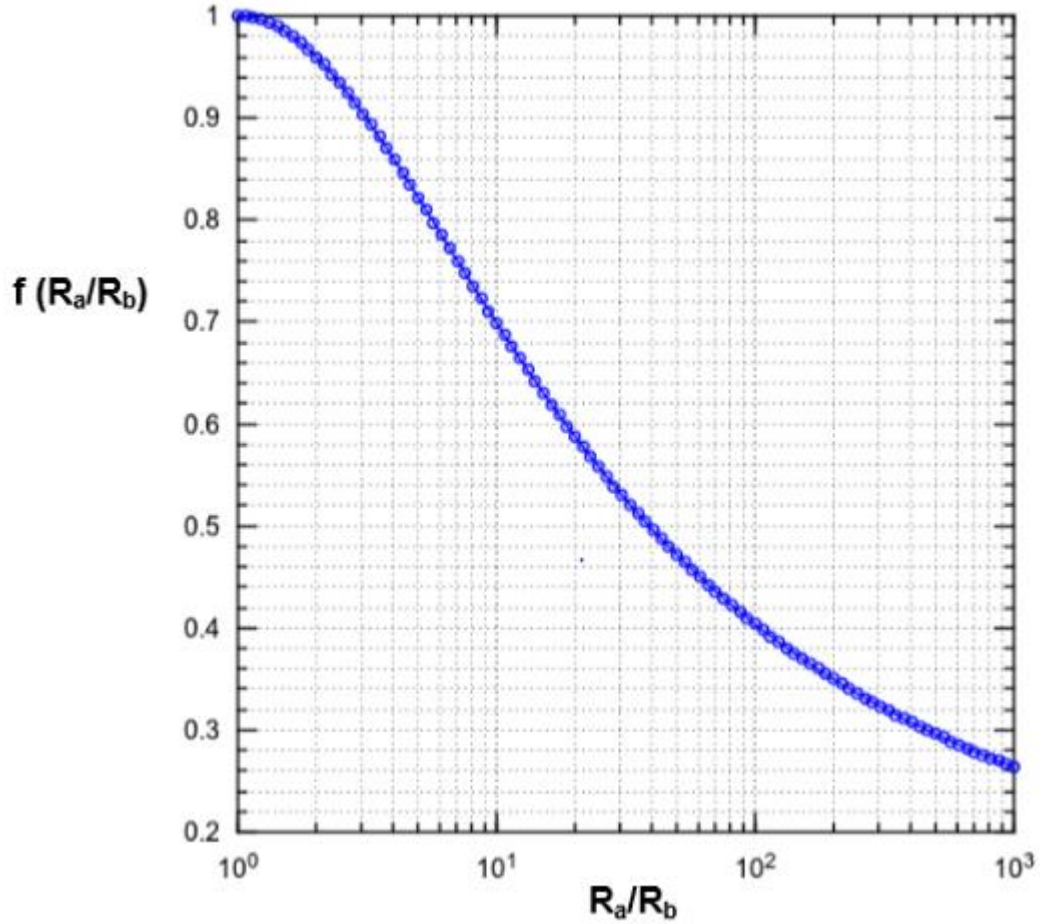


Figure 2.4: Graph of Van Der Pauw function.

### 2.2.2 Hall bar technique.

The hall bar sample consists of two contact points (current and voltage) is another technique to study the resistivity by using equation (2.27).

$$\rho = \frac{1}{\sigma} \quad (2.27)$$

Where;

$$\sigma = \frac{IL}{VA} \quad (2.28)$$

Where, ( $A$ ) is the cross-sectional area, ( $L$ ) is the length, ( $\rho$ ) is the electrical resistivity of the material and ( $\sigma$ ) is the electrical conductivity of the material.

Shown hall- bar geometry in Fig. 2.5, in which  $l$ ,  $w$  and  $t$  are the length, width and thickness of the sandwiched films, respectively.

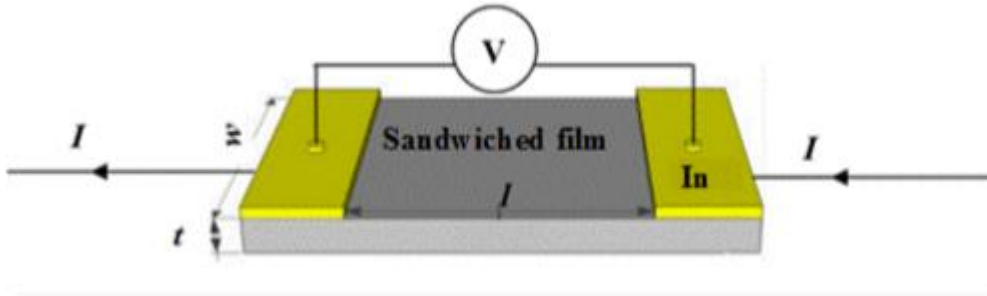


Figure 2.5: Hall- bar geometry.

### 2.3 Impedance Spectroscopy.

Impedance spectroscopy method to discover the electronic density of states in semiconductor materials. This process includes in mensuration of the charge transfer conductance, resistance, capacitance and another of a semiconductor interface at a different frequencies. It is a basic tool for studying semiconductor electronics, it includes information about the structure of the electronic interface [33].

### 2.3.1 AC Capacitance.

The AC capacitance is the capability to store electrical energy. It is the very significant part in several amorphous semiconductors and insulators, it is an important part to know the electrical structure of any appliance [34].

To derive the AC capacitance [35]:

$$C(\omega) = \frac{1}{\omega} \text{Im}[Y(\omega)] \quad (2.29)$$

And,

$$Y(\omega) = \frac{\delta I(\omega)}{\delta V(\omega)} \quad (2.30)$$

If this device have the small signal harmonic current and small signal voltage  $\delta I$  and  $\delta V \sim e^{i\omega t}$ . Let us consider transient current in a semiconductor device in response to an applied voltage is:

$$\delta V(t) = V(t) - V(0) = V\Delta\theta(t) \quad (2.31)$$

But transport current is:

$$\delta I(t) = I(t) - I(0) = [I(t) - I(\infty)]\theta(t) + [I(\infty) - I(0)]\theta(t) \quad (2.32)$$

Where  $\theta(t)$  is unity step function, The quantities of "+" and "-" superscripts denote single-sided values of the discontinuous functions for example:  $(0) = \lim_{t \rightarrow 0} V(t), t < 0$ , let the transient current equal  $\delta J(t) = [I(t) - I(\infty)]\theta(t)$  so that  $\delta J(t) \rightarrow 0$  at  $t \rightarrow \infty$ .

Substituting equation (2.31) & (2.32) in equation (2.30) and noting that  $\int_{-\infty}^{\infty} \theta(t)e^{i\omega t} dt = \frac{1}{i\omega}$ :

$$Y(\omega) = i\omega \int_0^{\infty} \delta I(t) e^{i\omega t} dt \quad (2.33)$$

Separated of real and imaginary part in equation (2.33) to get the formula of capacitance:

$$C(\omega) = \frac{1}{\Delta V} \int_0^{\infty} \delta J(t) \cos(\omega t) dt \quad (2.34)$$

In general:

$$\delta J(t) = C_0 \Delta V \delta(t) + \delta j(t) \quad (2.35)$$

Where  $C_0$  is the cold capacitance and  $\delta(t)$  is the delta function.

Rewrite equation (2.34) in terms of  $\delta j(t)$ :

$$C(\omega) = C_0 + \frac{1}{\Delta V} \int_0^{\infty} \delta j(t) \cos(\omega t) dt \quad (2.36)$$

Integrate equation (2.36) by parts and we get:

$$C(\omega) = C_0 + \frac{1}{\omega \Delta V} \int_0^{\infty} \left[ -\frac{d\delta j(t)}{dt} \right] \sin(\omega t) dt \quad (2.37)$$

The capacitance equation has a two parts ( $C_0$  and  $C_1$ ) where and by comparing equation (2.36)

& (2.37):

$$C_1 = \frac{1}{\Delta V} \int_0^{\infty} \delta j(t) \cos(\omega t) dt = \frac{1}{\omega \Delta V} \int_0^{\infty} \left[ -\frac{d\delta j(t)}{dt} \right] \sin(\omega t) dt \quad (2.38)$$

We assume two different frequency domains ( $\omega - \omega_n$ ) and ( $\omega - \omega_p$ ), where  $\omega_n$  and  $\omega_p$  are the domain frequency in the n-region and p-region, respectively [36]. After that we can rewrite equation (2.38) to become:

$$C_1 = \frac{1}{\Delta V} \int_0^{\infty} \delta j(t) \cos(\omega - \omega_{n,p})t dt = \frac{1}{\omega \Delta V} \int_0^{\infty} \left[ -\frac{d\delta j(t)}{dt} \right] \sin(\omega - \omega_{n,p})t dt \quad (2.39)$$

To explain these considerations, let us consider a simple general type of transient response composed of negative and positive exponential components:

$$\delta j(t) = \Delta V \left( a_n \exp\left(-\frac{t}{\tau_n}\right) - a_p \exp\left(-\frac{t}{\tau_p}\right) \right) \quad (2.40)$$

By substitute equation (2.40) in equation (2.39) and integrate us get:

$$C_1 = \frac{a_n \tau_n}{1 + (\omega - \omega_n)^2 \tau_n^2} - \frac{a_p \tau_p}{1 + (\omega - \omega_p)^2 \tau_p^2} \quad (2.41)$$

Where  $C(\omega) = C_0 + C_1$ , so that the final formula for the capacitance in terms of frequency is:

$$C(\omega) = C_0 + \frac{a_n \tau_n}{1 + (\omega - \omega_n)^2 \tau_n^2} - \frac{a_p \tau_p}{1 + (\omega - \omega_p)^2 \tau_p^2} \quad (2.42)$$

The AC capacitance depends on frequency, where ( $C_0$ ) is the geometrical capacitance, ( $a_n, a_p$ ) are assumed to be the parameter, ( $\omega_n, \omega_p$ ) are the Plasmon frequencies for n-type material and p-type material respectively, and  $\tau_0, \tau_n$  and  $\tau_p$  are the respective relaxation

times. Equation (2.42) assume that the semiconductor have self-compensation properties so that both carriers do exist in the material.

### **2.3.2 The reflection coefficient.**

Reflection coefficient ( $\rho$ ) is the capability of the device to transport or refuse AC signals. It also appears the quality of the impedance ( $Z$ ) between the film and the source. As the value of the reflection coefficient reduces the match between the film and the source increases [37]:

$$\rho = \frac{(Z - 1)}{(Z + 1)} \quad (2.43)$$

The impedance  $Z$  is measured an LCR meter.

### **2.3.3 The return loss.**

The return loss ( $L_r$ ) is the measure of the power that is not absorbed by the load and it returns back to the source and measured in dB and it is calculated from [38]:

$$L_r = -20 \log \rho \quad (2.44)$$

## Chapter Three

### Experimental Details

#### 3.1 Preparation of samples.

Thin films are prepared onto ultrasonically cleaned glass substrates which are cleaned by distilled water heat at temperature below 75°C for 40 minute. The slides were then taken out of the ultrasonic device and immersed in alcohol and dried using a hair dryer.

We prepared samples by using the evaporation source, An MoO<sub>3</sub> layer of thickness 500 nm was evaporated (figure 3.1).

For any deposition cycle, the following procedure can be followed:

- 1- Put the MoO<sub>3</sub> powder in the metal heating resistor (boat shaped) (item 1 in figure 3a).
- 2- Placed the glass substrates and Au metal and Van der Paw masks on the base metal (item 2 in figure a).
- 3- Put Au and Van der Paw masks with glass for later use in electrical measurement.
- 4- The shutter that covers the samples (item 3 in figure 3a) and the device is closed by the chamber (item 5 in figure 3b).
- 5- Check the connection between the software and the system to control the thickness monitor.



Figure 3.1: The physical vapor deposition system. a. from inside. b. from outside.

6- Start carrying out the physical vapor deposition technique, after locking the system and eliminating air inside by employing vent valve, and waiting the pressure to reach 10 mbar for operating the turbo pump.

7- When the vacuum reaches to  $10^{-5}$  mbar provide a current about 20 A and turn on the shutter with clockwise.

8- Two minutes after raising to the current 50A and increase the current to 60A and open the shutter so until the thickness of 500 nm, (item 4 in figure a).

9- After the MoO<sub>3</sub>/In interface has formed Indium the second cycle of evaporation, Indium was attended in five evaporation.

10- The evaporated Indium films of thickness of 0, 50, 75, 100 and 200 nm onto MoO<sub>3</sub> thin film bases gradually.

11- The obtained interfaces were applied as a new base for the evaporation of another 500 nm MoO<sub>3</sub>. The final form MoO<sub>3</sub>/In/MoO<sub>3</sub> (MIM-d (nm)) nanosandwiching films as appeared (figure 3.2 and figure 3.3).

### **3.2. The geometrical shape and optical image nanosandwiching films.**

For the electrical characterizations, the manufacturing of MoO<sub>3</sub>/In/MoO<sub>3</sub> requires the metal substrate instead of glass. Gold permit an electrical contact to the semiconductor the application of electrical fields shown in figure (3.2, 3.3). After getting Au/MoO<sub>3</sub>/In/MoO<sub>3</sub> films, the Au contacts were deposited onto the film surface to form ohmic/rectifying contacts utilizing suitable masks. The conductive gold point contacts were deposited on the surface of the films shown in figure 3.4.

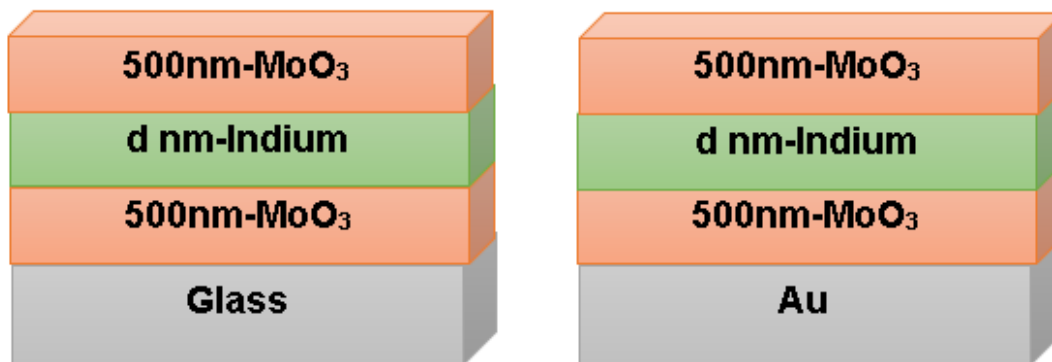


Figure 3.2: The geometrical design of MIM and Au/MIM thin films.



Figure. 3.3 optical image nanosandwiched films  $d=0, 50, 75, 100$  and  $200\text{nm}$ .

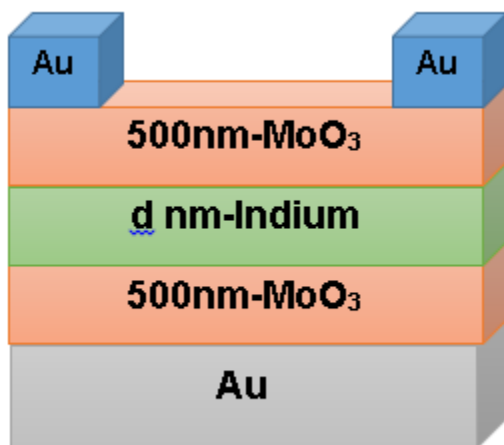


Figure. 3.4: The geometrical design of Au/MIM/Au thin films.

### 3.3 X- ray diffraction (XRD) measurements.

We used the device that named Rigaku Miniflex 600 diffractometer (figure 3.5) to measure the X-rays of the samples which includes MIM thin films and Au/MIM for all thicknesses, the samples were measured in the angle range of  $10^{\circ}$ - $70^{\circ}$  with scan rate was  $1^{\circ}/\text{min}$  and the step size of  $0.5^{\circ}$ . We used TREOR-92 computer program to analyze the X-ray patterns and even find the structure parameter for samples.



Figure. 3.5: Rigaku Miniflex 600 diffractometer.

XRD is the accurate analytical method used for determining the crystalline nature of the substance, (wavelength equals  $1.5405 \text{ \AA}$ ). So the X rays is unique to study the crystalline properties of the material because the wavelength of the convergence of the distance between atoms and between levels and therefore possible to get an interference and diffraction. Using the Bragg's law in section (2.1.1) to get the intensity of a diffract X-ray beam as a function

of angle. The device consists of the following basic parts: (a) Source of X-ray. (b) Collimator. (c) Detector. (d) Holder. (e) Signal processor. (figure. 3.6)

The principle of machine operation is based on the standard tools which used a line focus x-ray tube (most of their consist of Cu-radiation), Soller-slits and collimators to determine the beam divergence. It is also used to limit the wavelength range .The diffractometer is turned on a detector rotation and running in  $\theta/2\theta$  mode for the samples and a symmetrical radiation. The flat multilayer monochromators (Göbel-Mirrors) can be tuned to any wavelength with some minor changes in the path of the primary radiation, this allows a quick modification of wavelengths to improve the breakthrough depth for a high signal [39].

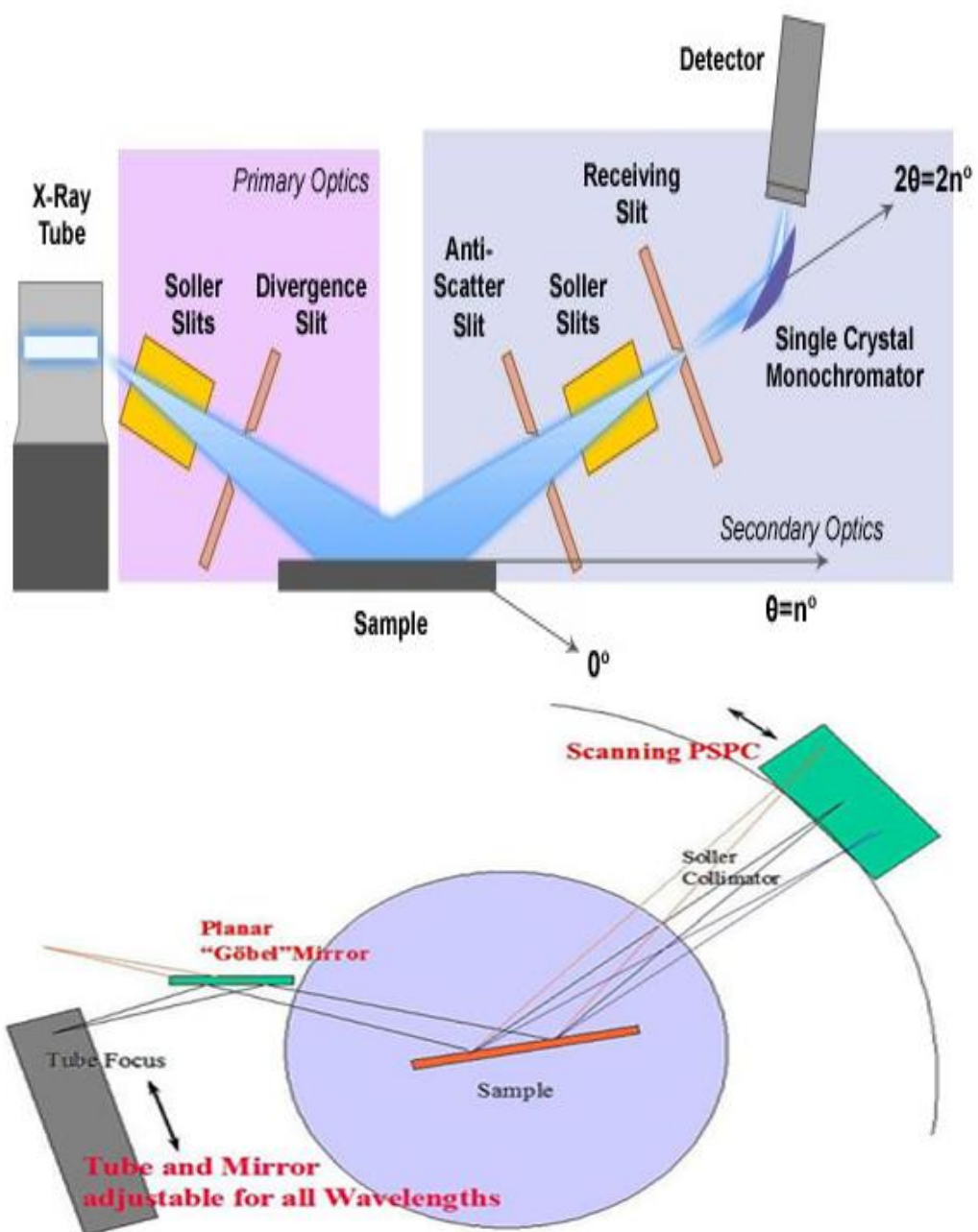


Figure. 3.6: Schematic view of Bragg-Brentano system.

### 3.4 The Impedance measurements.

The impedance spectroscopy was measured at room temperature of 300 K in the frequency range of (10 MHz -1.8 GHz) using the device shown in figure 3.7 which is called Agilent 4291B impedance analyzer the operation principle is to insert an electric field (AC signal ) on the RLC circuit.

We placed a small point of carbon on the samples and then we put the samples (Au/MIM/ C) into the device and used the MATLAB program to control the measure of the samples, the device calculates a lot of parameters include impedance (Z), resistance (R), reactance (X), conductance (G) and reflection Coefficient  $|\Gamma|$ .

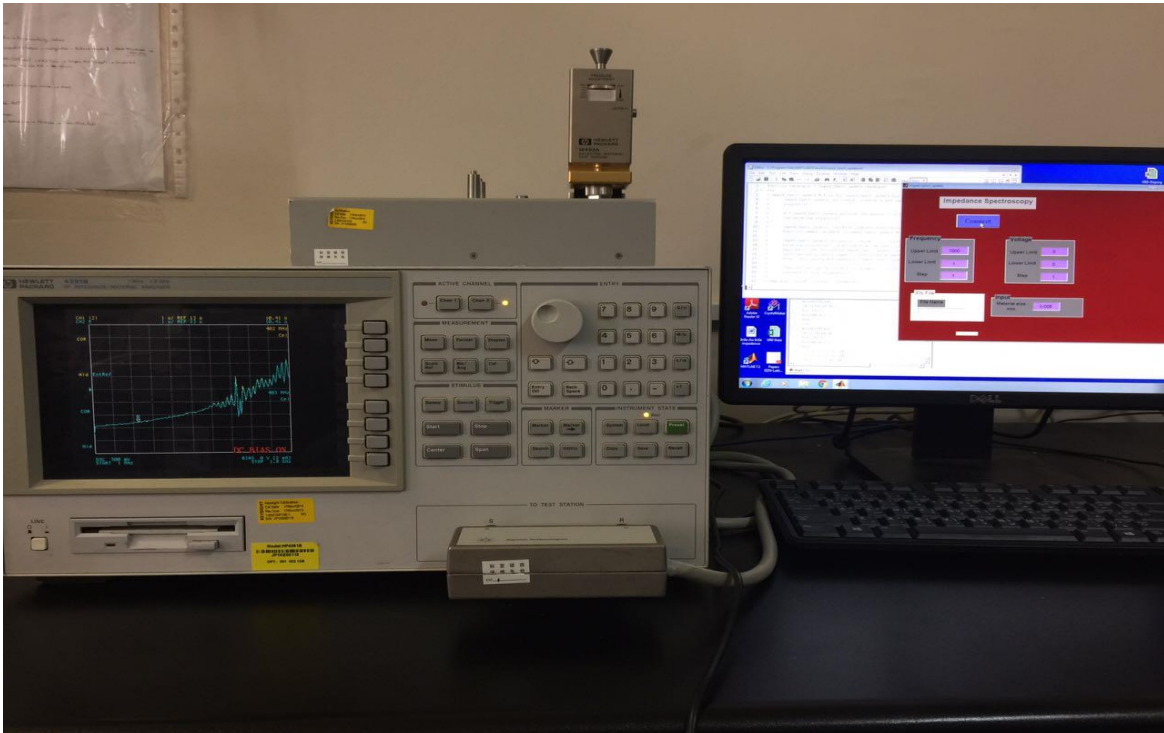


Figure 3.7: Agilent 4291B 1.0 M-1.8 GHz impedance analyzer.

### **3.5 The electrical measurements.**

We used the Keithley 230 as a voltage source, Keithley 6485 picoammeter (figure 3.8) to measure the (I–V) characteristics of the samples ( Hall bar and Van der Paw) ,the electrical connection was obtained from points of gold deposited on the sample using the evaporation device as discussed in section 3.1.

MATLAB program was used to control the voltage and current of the samples at different temperatures. The samples were mounted on a holder. The holder is surrounded by copper wire connected with the devices in order to increase the temperature of the sample. A k-type thermocouple is fixed on the top of the sample to monitor the temperature through digital multimeter that allow readily k-type thermocouple, so that the voltage is constant and equals 100V.



Figure. 3.8: Electrical measurement setup.

Hall bar samples were measured as shown in figure 3.9 where we placed sample whose length is four times the width on a glass base and placed two copper wires on the sample and fixed the wire in a piece of glass and put a little silver on the wire and on the part of the sample for electrical contact.

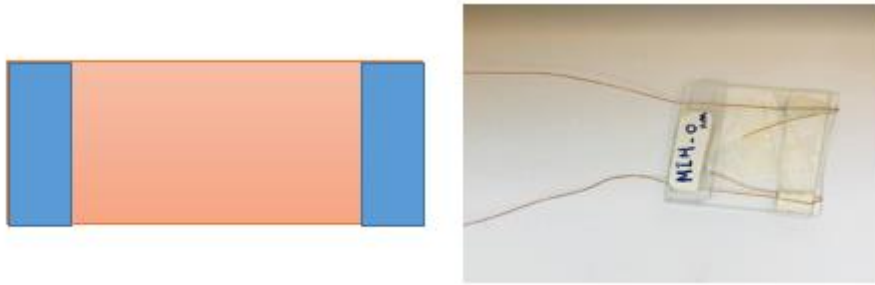


Figure. 3.9: The hall bar design.

Van der Paw samples were measured as shown in figure 3.10 where we placed four copper wires on the points of contact (gold points) and fixed the wires by the welded-indium, and we connected the wires in points 1 and 4 with the current and connect wires in points 2 and 3 with the voltage and read the measurements.

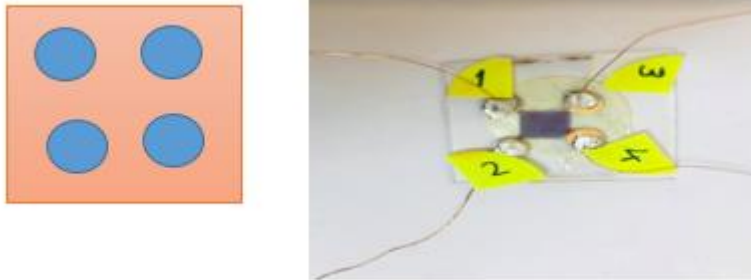


Figure. 3.10: The van der Paw design.

### 3.6 The "hot-probe" technique.

The "hot-probe" technique which is shown in figure 3.11 was applied to differentiate between n-type and p-type employ a heater with temperature  $\sim 450\text{ C}^\circ$  and a standard digital multimeter (DMM), the hot-probe technique is that defined the conductivity type of semiconductors. In this technique the hot iron is linked to the positive terminal of the multimeter while the cold one is linked to the negative terminal, if the DMM is reading out positive voltage then the semiconductor is an n-type, but p-type if the voltage negative. As an explication for this experience when the heater connected the surface, thermally raised majority free charged carriers are spread during the semiconductor from the hot to the cold probe. These explicit majority carriers limited the electrical potential sign in the multimeter. Thus, the hot probe surround zone be charged with minority carriers but cold probe remains neutral [40].

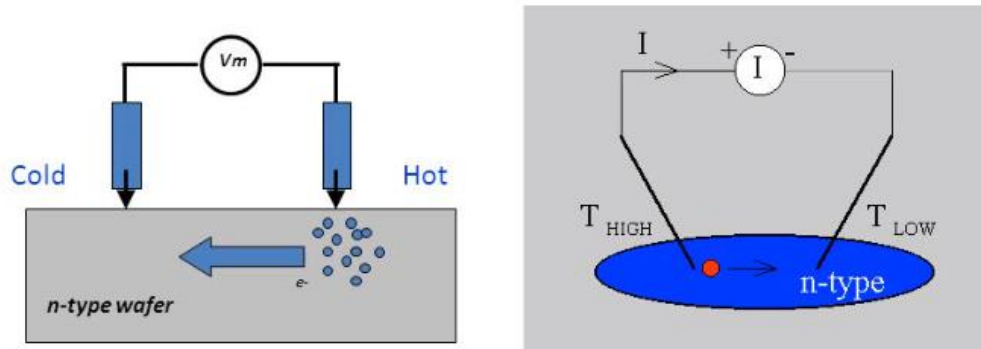


Fig. 3.11: Experimental set-up of the "hot-probe" experiment.

## **Chapter Four**

### **Results and discussion**

#### **4.1 Structural analysis.**

In this chapter we discuss the results that emerged from thin films of MoO<sub>3</sub>/Indium/MoO<sub>3</sub> (MIM) and Au/MIM. The thickness of indium layer was varied in the range of 50-200 nm. The crystalline and nature of the films will be explored by means of x-ray diffraction. The structural analysis will take into account the films which are prepared onto glass and onto metal substrate.

##### **4.1.1 MoO<sub>3</sub>/In/MoO<sub>3</sub> films grown onto glass substrate.**

The X-ray diffraction patterns are measured for the MIM samples of different thicknesses (0, 50, 75, 100 and 200 nm) and for an indium sample at room temperature. When the thickness of indium is increased, the crystalline structure improves as illustrated in Fig 4.1. There is no peaks for MIM-0 nm and MIM-50 nm, so that it is amorphous structure because the gross volume of the grain is minimal [41]. MIM 0, 50 nm are amorphous so that the size of oxygen vacancy is so large. As a result, the deformation in the MIM sample, is expected to be large [42].

As seen from Fig 4.1, there is one peak for MIM-75nm and MIM-100nm so that they are polycrystalline structure. The peak for MIM-75 nm occurs at  $2\theta = 33.75^\circ$  and the peak for MIM-100 nm occurs at  $2\theta = 33.45^\circ$ . These peaks referred to tetragonal indium, (we used a TREOR 92 X-ray diffraction program to analyze the pecks). MIM-200 nm is also of

crystalline structure with three peaks, the first peak occurs at  $2\theta = 30.4^\circ$ , the second peak which has the maximum intensity occurs at  $2\theta = 33.65^\circ$ , these peaks also referred to indium tetragonal, however, the last peak occurs at  $2\theta = 37^\circ$  referred to the orthorhombic phase of  $\alpha$ - $\text{MoO}_3$  [43]

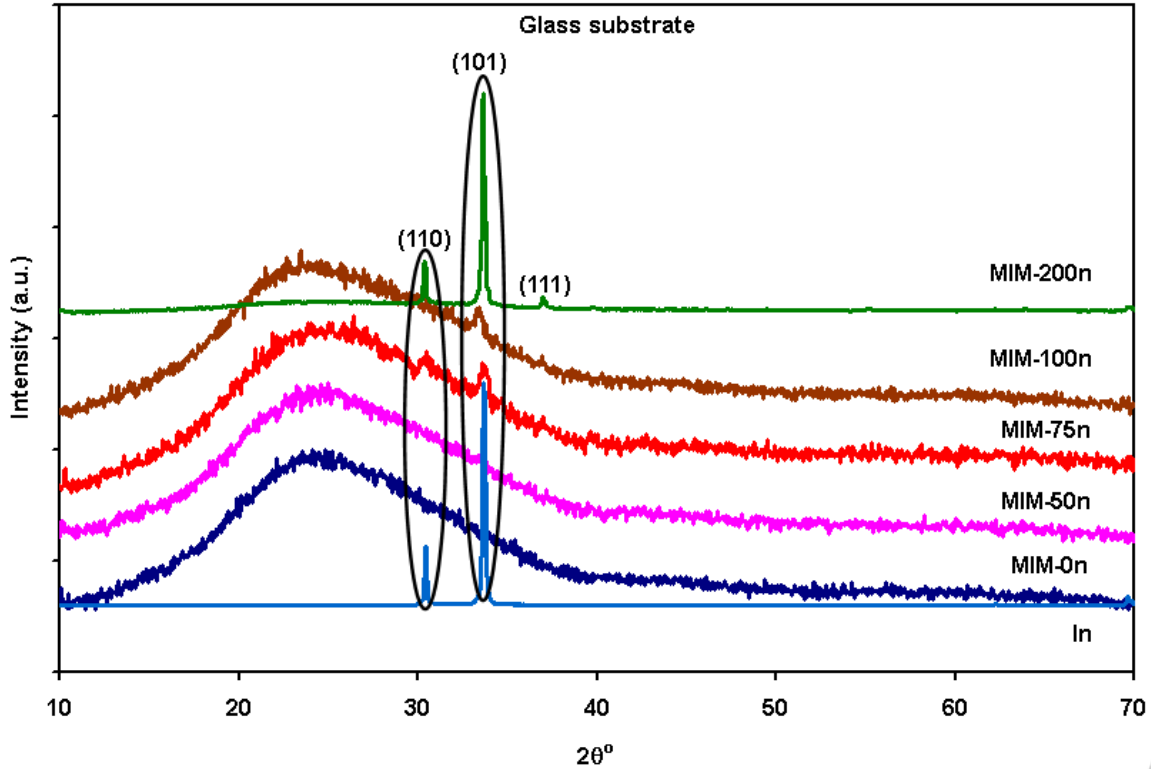


Figure 4.1: XRD pattern of indium metal and the (MIM) sandwiched films  
(Measured at room temperature).

The lattice parameters are calculated using the "TREOR 92" software. Table 4.1 shows mechanical parameters for MIM-75 nm, MIM-100 nm and MIM-200 nm. That were calculated using equations (2.16-2.17).

Table 4. 1: Mechanical parameters for MIM-75 nm, MIM-100 nm and MIM-200 nm.

Parameter	Symbol	MIM-75 nm referred to In	MIM-100 nm referred to In	MIM-200 nm Referred to In	MIM-200 nm referred to MoO <sub>3</sub>
Angle	$2\theta$	33.75	33.45	33.65	37
Intensity	I (a.u.)	997	1398	19939	1719
FWHM	$\beta$ (rad)	0.009071	0.001744	0.002617	0.003489
Grain size	D (nm)	16	86	57	43
Strain	$\times 10^{-3}\epsilon$	7.4	1.4	2.1	2.6
Stacking faults	SF%	41.6	8.0	12.0	15.2
Dislocation density	$\delta a$ ( $\times 10^{11}$ line/cm <sup>2</sup> )	20.6	0.77	1.72	2.25
Dislocation density	$\delta b$ ( $\times 10^{11}$ line/cm <sup>2</sup> )	-	-	-	0.64
Dislocation density	$\delta c$ ( $\times 10^{11}$ line/cm <sup>2</sup> )	13.5	0.50	0.13	2.41
Lattice parameter	a(A°)	3.25	3.25	3.25	3.97
Lattice parameter	b(A°)	-	-	-	13.90
Lattice parameter	c(A°)	4.947	4.947	4.947	3.69

In table 4.1, in the description of Indium peaks, we observed that the intensity of indium increases when the thickness for indium layer increases. The grain size of indium in MIM-75 nm equals 16.6 nm then it increase in MIM-100 nm to 86.6 nm, thereafter its decreases to 57.8 nm.

The strain, stacking faults and dislocation density parameters for indium decreases for MIM-100 nm, then its increases in MIM-200 nm, even though, the lattice parameters remain constant. Pointing out that there is one peak occurs at  $2\theta = 37^\circ$  referred to  $\alpha\text{-MoO}_3$ . The decrees in the grain size of the indium layer upon growth of  $\alpha\text{-MoO}_3$  is assigned to the stress caused by the formation of regular grains in the structure of top layer of MIM samples.

To understand the changes that have happened in the former values for each of D, SF and  $\delta$ , it has been taken into account many factors (deformation, critical thickness and lattice mismatch). Because O<sub>2</sub> atoms in MoO<sub>3</sub> include much vacancies and random configuration of atoms, so when we add indium, it will not place the atoms in the appropriate place. It means that there is defect in the configuration of atoms within the MIM, which results in changing values of D, SF and  $\delta$  [44, 45].

To explained the nano-sandwiching impact on the structure of the films, we observe the distribution of Mo vacancies is useful. Oxygen ion (O<sup>+6</sup>) has an ionic radius of 1.40 Å [46] which is larger than that of Mo ion (Mo<sup>+6</sup>)0.59 Å [47] and indium ion (In<sup>+3</sup>)0.94 Å [48]. Thus the substitution of indium in the Mo site can be excluded, while the interaction of O with indium and the formation of In<sub>2</sub>O<sub>3</sub> should also be considered. It is possible for the In<sup>+3</sup> ion to replace the vacant sites of Mo<sup>+6</sup> and form In<sub>2</sub>O<sub>3</sub> bonds. The formation of this bond would acquire more oxygen atoms because the In<sup>+3</sup> ion (acceptor impurity) provide an extra

hole due to its deficiency in valence electrons. Also, the bond length of Mo-Mo is 2.419 Å [49] and the bond length of the Mo-O<sub>1</sub> is 1.71 Å [50]. The bond length of Mo-O<sub>2</sub> is 1.98 Å [50]. The bond length of Mo-O<sub>3</sub> is 1.98 Å [50]. The bond length of In-Mo is 2.739 Å [51]. The bond length of In-O is 2.12-2.21 Å [52]. Mo-O<sub>1</sub> bonds are shorter than In-O bonds indicating that MoO<sub>3</sub> electronic transition should be preferred over In<sub>2</sub>O<sub>3</sub> transition. However, because the X-ray patterns did not display intensive peak that relate to the In<sub>2</sub>O<sub>3</sub>, it is possible to accept that the MoO<sub>3</sub>/In/MoO<sub>3</sub> sandwiched structure is mostly of physical type (substitutional and/or interstitial). With these features, the indium film can be mostly regarded as a metallic slab being inserted between two layers of MoO<sub>3</sub>. Generally, The Mo vacancies and interstitial oxygen are reported to act as acceptors, while oxygen vacancies and interstitial Mo act as donors [53].

#### **4.1.2 MIM samples prepared onto Au substrate.**

The same previous study was repeated with a change of substrate from glass (amorphous material) to Au (crystalline material) thin film. Figure (4.2) shows the XRD pattern for Au-MIM at different thicknesses of indium.

We used crystalline surface (Au) to stimulate the formation of another crystal, but this only happened when indium high thickness, where at adding the indium after a certain level turns the material from amorphous to crystal and when adding more indium becomes a better crystal.

The Au-MIM-0 nm has five peaks; four of them referred to Au with cubic structure at  $2\theta = 35.2, 39.00, 45.3, 65.55^\circ$  in different orientations, whereas the fifth peak occurs at  $2\theta$

$=23.15^\circ$  with orientation of (110) which referred to  $\alpha$ - $\text{MoO}_3$ . The Au-MIM-50 nm and Au-MIM-75 nm have four peaks that referred to Au. Au-MIM-100 nm has five peaks, four of them are the same as Au-MIM-75 nm and a new peak is referred to indium which accrues at  $2\theta = 33.6^\circ$  with (101) orientation. Au-MIM-200 nm has three new peaks (when it is compare with MIM -50 nm), two of them referred to  $\alpha$ - $\text{MoO}_3$  at  $2\theta = 37.00^\circ$  and  $2\theta = 55.3^\circ$  and the third peak referred to indium at  $2\theta = 30.4^\circ$  with (110) orientation.

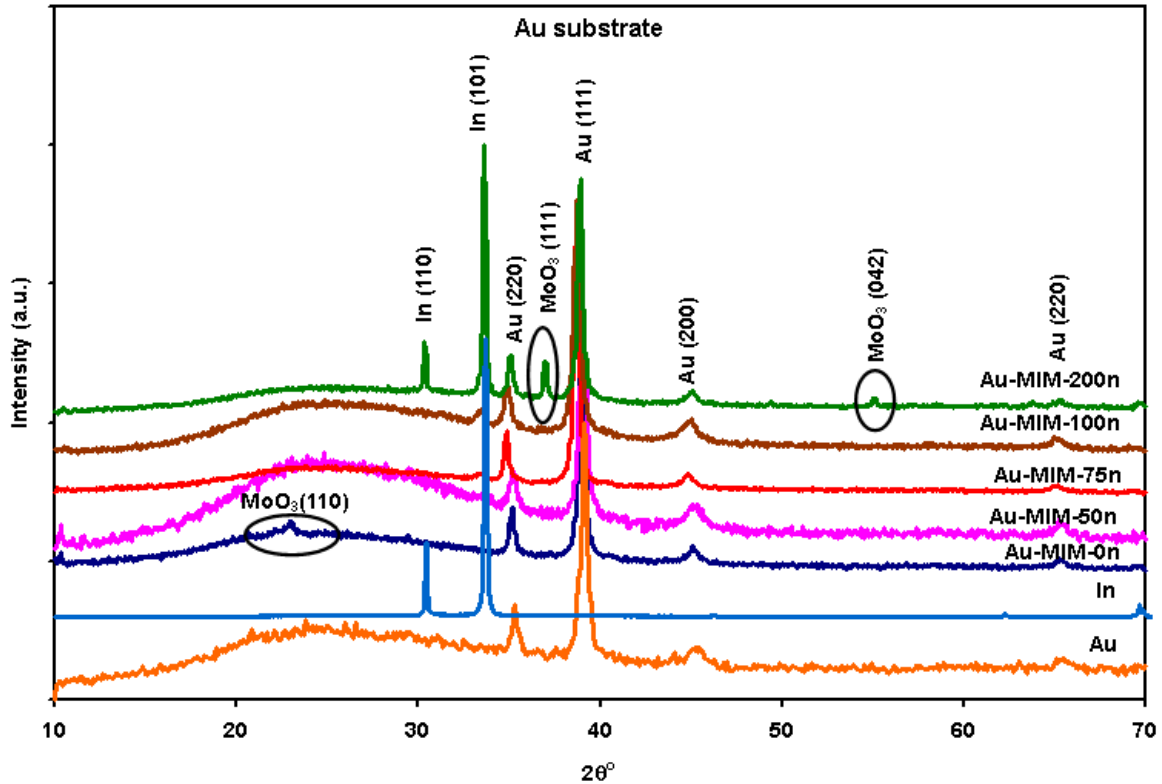


Figure 4.2: XRD pattern of Indium (In), gold (Au) metals and the (Au/MIM) sandwiched films measured at room temperature.

Table 4.2 shows the x-ray diffraction parameters for Au-MIM-200 nm. It has been described MoO<sub>3</sub> peaks. We observed that the intensity for MoO<sub>3</sub> decreases when the angle increases. The grain size (D) in Au-MIM-200 nm at  $2\theta = 37.00^\circ$  equals 29 nm then it increase at  $2\theta = 55.3^\circ$  equals 187.4 nm.

The strain, stacking faults and dislocation density parameters for MoO<sub>3</sub> decreases, even though, the lattice parameters remain constant.

Table 4.2: Mechanical parameters for  $\alpha$ -MoO<sub>3</sub> and Au for Au/MIM-200 nm.

Parameter	Symbol	Au-MIM-200 nm at $2\theta= 37$	Au-MIM-200 nm at $2\theta= 55.3$	Au-MIM-200 nm at $\theta= 35.152$	Au-MIM-200 nm at $2\theta= 38.9$	Au-MIM-200 nm at $2\theta= 45.35$	Au-MIM-200 nm at $2\theta= 65.55$
Material	-	MoO <sub>3</sub>	MoO <sub>3</sub>	Au	Au	Au	Au
Intensity	I (a.u.)	2072	675	2055	8371	862	711
FWHM	$\beta$ (rad)	0.005233	0.000872	0.005233	0.006106	0.019189	0.009594
Grain size	D (nm)	29.17	187.4	29.02	25.15	8.17	17.9
Plane direction	Hkl	111	042	220	111	200	220
Strain	$\times 10^{-3}\epsilon$	3.9	4.1	4.1	4.3	11	3.7
Stacking faults	SF%	22.8	3.0	23.5	26.0	75.1	30.2
Dislocation density	$\delta a$ ( $\times 10^{11}$ line/cm <sup>2</sup> )	5.0	0.08	5.2	6.3	51.0	9.0
Dislocation density	$\delta b$ ( $\times 10^{11}$ line/cm <sup>2</sup> )	1.4	0.02	-	-	-	-
Dislocation density	$\delta c$ ( $\times 10^{11}$ line/cm <sup>2</sup> )	1.4	0.02	-	-	-	-
Lattice parameter	a(A°)	3.97	3.97	4.08	4.08	4.08	4.08
Lattice parameter	b(A°)	13.90	13.90	-	-	-	-
Lattice parameter	c(A°)	3.69	3.69	-	-	-	-

From chemical point of view, the ionic radius of  $Au^+$  is  $0.0137 \text{ \AA}$  [54] smaller than for  $O^{+6}$  and  $Mo^{+6}$  [49]. In this case, the substituting of  $Au^+$  in  $O^{+6}$  or  $Mo^{+6}$  sites is possible and substitution of  $Au^+$  ions between Mo-Mo bonds to form Au-Mo bonds may have occurred. The Au metal belongs to  $F_{m-3m}$  space group and exhibit an FCC structure of lattice constant  $4.08 \text{ \AA}$  [54], which indicates a lattice mismatch in table 4.3. Although large lattice mismatched heterojunctions causes high performances in solar energy transformations, it may lead to relaxation via the generation of dislocations. The formation of such dislocations that behave as minority carrier recombination centers which reduce the performances [54] of photovoltaic materials is reduced by the nanosandwiching of indium between layers of  $MoO_3$ .

Table 4.3: Lattice mismatch between  $\alpha$ - $MoO_3$ , indium and Au slab.

All samples	Lattice mismatch ( $\Delta_1$ )	Lattice mismatch ( $\Delta_2$ )	Lattice mismatch ( $\Delta_3$ )
	22%	18%	2.7%

## 4.2 Electrical Characteristics.

The electrical conduction plays a significant role in the investigation of the semiconductor devices. In this section, the samples of Van Der Pauw and Hall bar are measured as function of temperature. Having evaluated the room temperature I-V characteristic, the samples were then subjected to a heating and cooling processes while monitoring the heating ( $I_H$ ) and cooling ( $I_C$ ) currents. The behavior and value of  $I_H$  and  $I_C$  are the same, therefore the average current for all samples is taken as ( $I_{av}$ ). During measurements, the van der pauw technique is

implemented using points 1 and 4 the current ( $I_{14}$ ), and points 2 and 3 for the voltage ( $V_{23}$ ) as shown in figure 3.10. In addition, the hall bar sample consists of two contact points (current and voltage) as shown in figure 2.4.

#### 4.2.1. I-V response of Van Der Pauw and Hall bar MIM films.

The current voltage characteristic are measured at room temperature for Van Der Pauw MIM-samples with thicknesses of 75, and 100 nm. Figure 4.3(a) shows the I-V characteristic MIM-75 nm which exhibits ohmic behavior. Also, figure 4.3(b) shows the I-V characteristic for MIM-100 nm whose behavior is also ohmic. The current of MIM-75 nm is less than ten times of the current of MIM-100 nm, this shows how the sample conductivity is improved by doping, so that the current for MIM-75 nm increase ten times when the indium thickness raised to 100 nm ( the slope  $(\frac{1}{R})$  for MIM-100 nm equal ten times for the slope 75 nm).

Whereas increases indium thickness, the valance electrons in the indium are increased and the free electrons are increased so the conductivity increases.

The Ohmic nature of the contact predominates when the work function of the metal is less than the work function of the semiconductor of n-type ( $q\phi_m < q\phi_{sm}$ ). This is expected for indium ( $q\phi_m = 4.09 eV$ ) [44], which is less than that of  $MoO_3$  ( $q\phi_{sm} = 4.36eV-4.95eV$ ) [55].

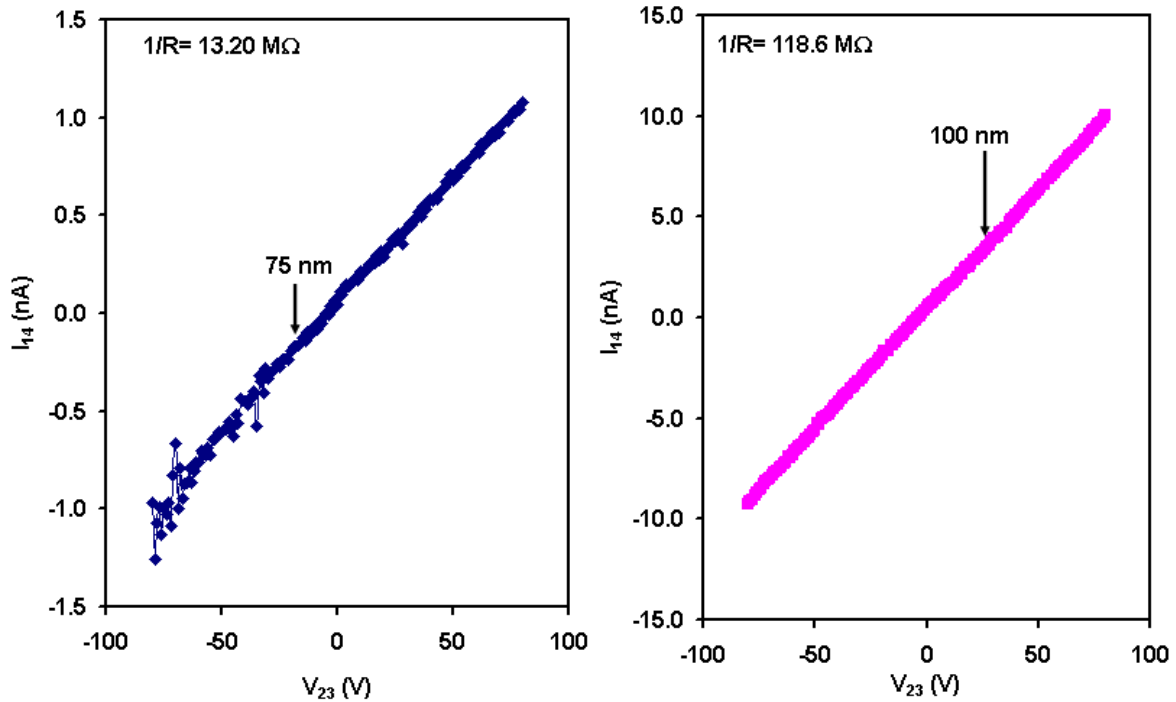


Figure 4.3. I-V response of Van Der Pauw MIM with thickness 75 and 100 nm of indium at room temperature.

Figure 4.4 shows I-V response, the current versus voltage is measured with Hall Bar technique for all samples with different thicknesses (0, 50, 75, 100 and 200 nm) of indium. The measured current is in the range of nano ampere (nA) for all samples except MIM-200, it is in the micro ampere ( $\mu\text{A}$ ) range (inset of Fig 4.4). For all samples the current increases with increasing the voltage in different ranges, began with MIM-0 nm the current increase gradually when the MIM samples increases expect the MIM-75 nm, the increases of current for which is less than the increases of current MIM-50 nm.

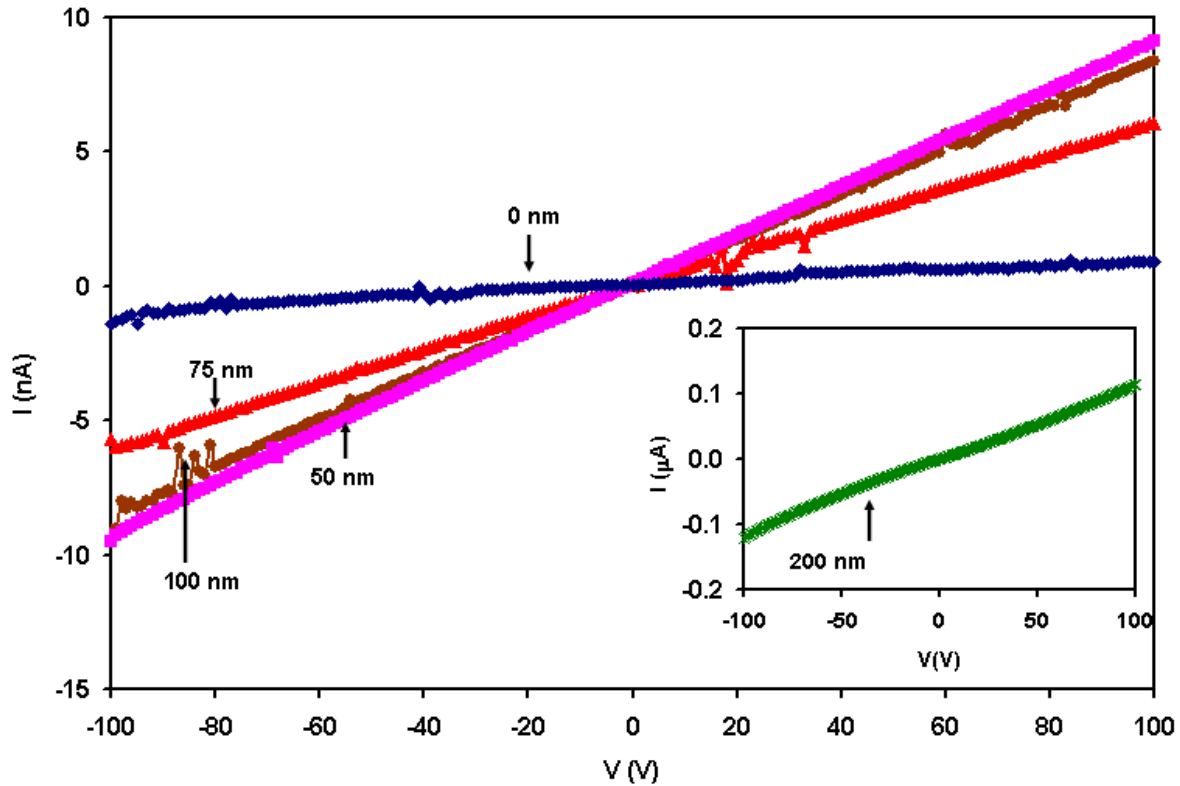


Figure 4.4. I-V response of Hall bar MIM all samples as grown at room temperature.

This can be explained by XRD, for MIM-75 nm sample, a peak appears and explains that the material is transformed from amorphous to polycrystalline. However, for this sample, the crystallinity of indium is still not dominant which means that there exist mixed structure composed of amorphous and polycrystalline material. The crystallinity of indium indicate that a physical layer of indium start to form, this make transition of free charge carries controlled by the indium inside the sample, while the MIM-100nm sample crystallinity was more pronounced, so then turns from amorphous to crystals. Thus, there's grain growth. The layer the grains the narrower the barrier at the grain boundaries the higher the current [56]. For MIM-0 nm, there is no indium, it is semi insulator, which has very low current. XRD explains this mechanism, we observed that the material was amorphous structure, random distribution

and the degree of disorder is very high, so that the resistivity becomes very high. The lower resistivity or better conduction appears when materials make transition from amorphous to polycrystalline. During the phase transition some of the grains melt grater forming greater grains orient to lower the barrier height during this process some of the many far from each other should be a reason for the current reduction [56].

#### 4.2.2 Comparison between van der pauw and hall bar technique to calculate the conductivity.

Conductivity is calculated with van der Paw technique using equation (2.24). In addition, it is calculated with Hall bar technique using equation (2.27). The calculated conductivity using both technics result in the same order of magnitude and the same trend of variation as shown in Table 4.4 and figure 4.5.

Table 4.4 The conductivity for all samples MIM at room tempreture.

Thickness	$\sigma(\text{VDP})$	$\sigma(\text{HB})$
MIM-50 nm	$5.8 \times 10^{-9}$	$2.1 \times 10^{-9}$
MIM-75 nm	$3.8 \times 10^{-9}$	$1.8 \times 10^{-9}$
MIM-100 nm	$7.4 \times 10^{-9}$	$2.2 \times 10^{-9}$
MIM-200 nm	$4.3 \times 10^{-6}$	$2.2 \times 10^{-6}$

Figure 4.5 shows the conductivity ( $\sigma$ ) versus temperature using van der pauw and Hall bar. The conductivity increases as the temperature increases. The increases of conductivity results

with increasing temperature is assigned to the freedom of charge carriers by thermal assistance [57]. The slight numerical difference in the values of electrical conductivity can be assigned to the Jeule effect as well as nerst's effect which affect the electrical conduction. Having a look on the curves which are shown in Fig 4.5, one can guess that the thicker the indium the closer the conductivity value. This indicate that there is main effect of indium distribution in the sample. The Hall Bar technique only will be used in calculating the rest of electrical parameters since there is almost no difference between van der pauw and Hall bar techniques.

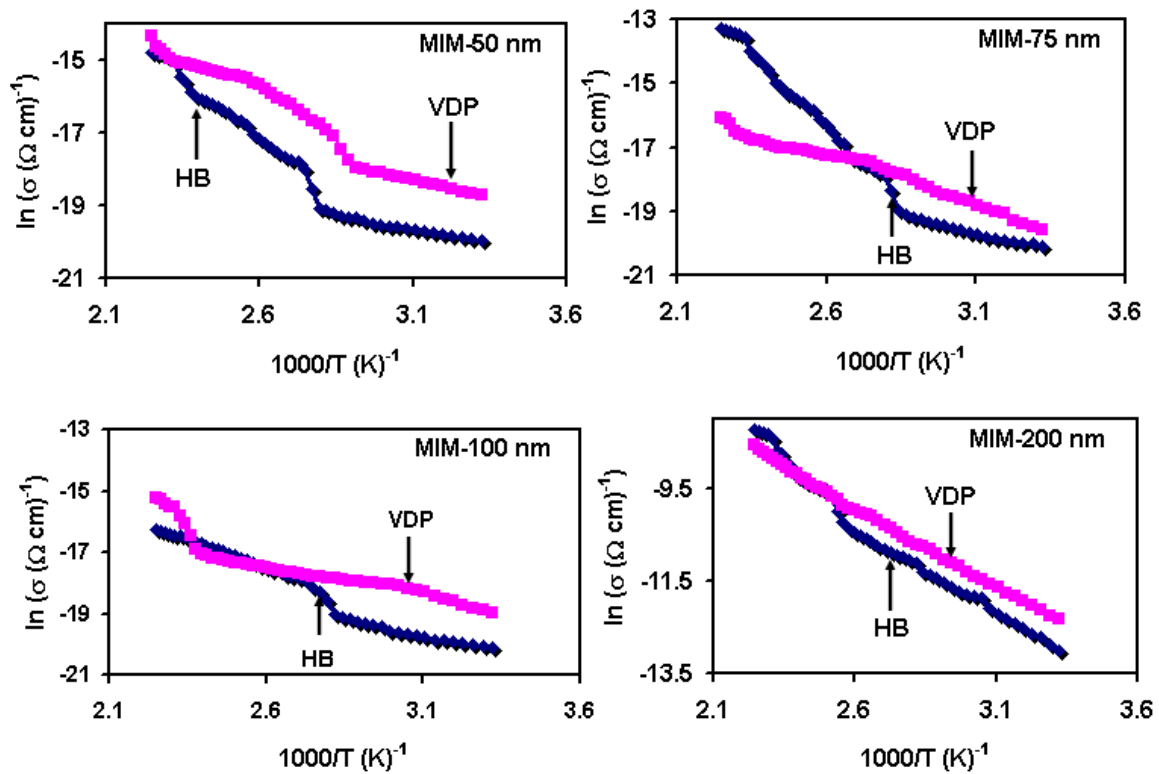


Figure 4.5. Conductivity of van der pauw and Hall bar of all samples MIM.

### 4.2.3 Effect of indium on electrical conductivity.

Table 4.4 shows the conductivity for MIM-samples. The conductivity is decreases from  $2.1 \times 10^{-9} (\Omega \cdot \text{cm})^{-1}$  to  $1.8 \times 10^{-9} (\Omega \cdot \text{cm})^{-1}$  as the thickness of indium increases from MIM-50 nm to MIM-75 nm, then at MIM-100 nm there is increases in the conductivity, after that when the thickness is increases to MIM-200 nm the conductivity is more increase  $2.2 \times 10^{-6} (\Omega \cdot \text{cm})^{-1}$  .

In order to understand the interfacing nature between the  $\text{MoO}_3$  and indium. The improved electrical conductivity in the electronic orbital distributions in the  $\text{MoO}_3$  and indium metals. The electronic configuration of Mo is  $1s^2 2s^2 2p^6 3s^2 3p^6 3d^{10} 4s^2 4p^6 4d^5 5s^1$  [58] while that of oxygen is  $1s^2 2s^2 2p^4$  [59] while that of indium  $1s^2 2s^2 2p^6 3s^2 3p^6 3d^{10} 4s^2 4p^6 4d^{10} 5s^2 5p^1$  [60]. Since the energy level of  $5p^1$  states are higher than  $5s^1$  and energy level over lapping take place. This makes the bonding between indium and  $\text{MoO}_3$  much powerful make free electron movement easier. Since the electrons are now at higher levels it is probably that the conductivity increases by forming impurity bands that are created by indium. Increasing the thickness of indium increases number of free electrons in the material which make the surface charge more overcrowded and the impurities level is shifted closer to the conduction band as result of state filling so the conductivity increasing.

### 4.2.4 Temperature dependent conductivity.

Figure 4.6 shows the conductivity versus temperature ( $\sigma$  Vs T (K)). The conductivity increases as the temperature increases. The behavior of increasing of conductivity is

following the trend of exponential function. Furthermore, it is shown that the conductivity conforms Arrhenius behavior which can be regarded as a semiconducting transport conduct [61].

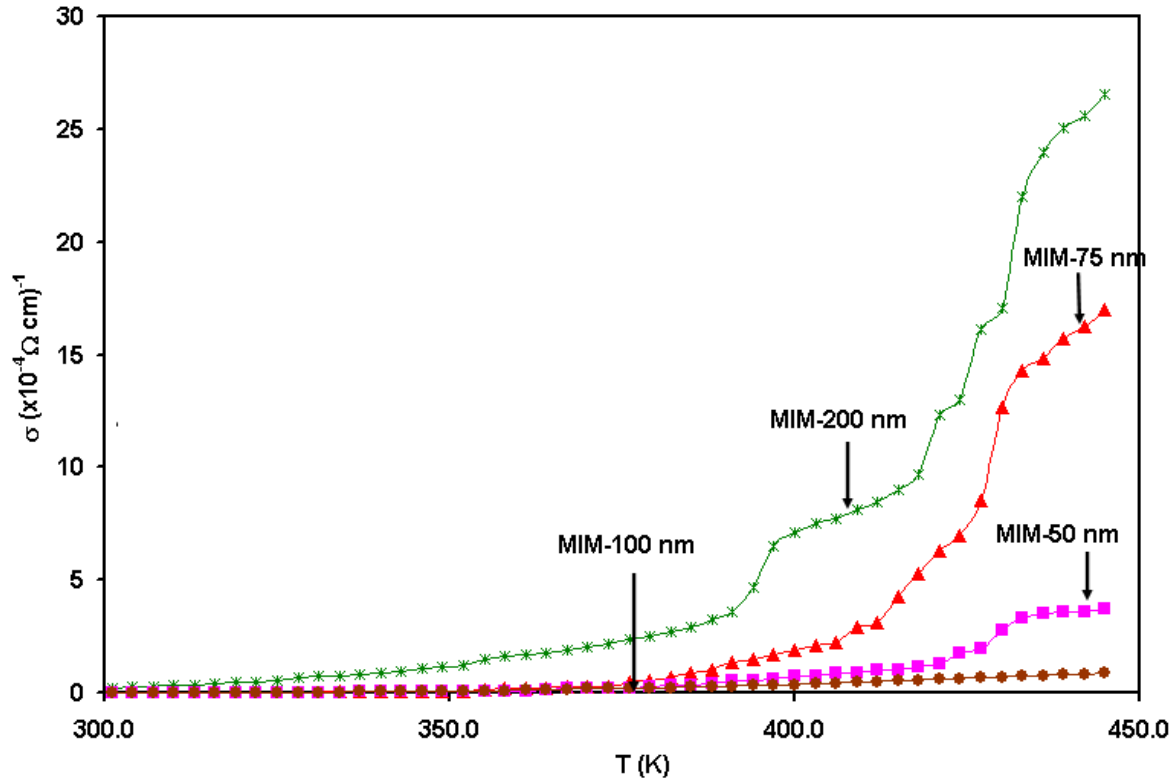


Figure 4.6 the conductivity of Hall bar for all samples  $\delta$  Vs T (K).

Figure 4.7 shows the logarithmic conductivity versus temperature T (K) using Hall bar technique. This figure shows the change of the samples from insulator to semiconductor as the temperature increases. At the point of change from insulator to semiconductor, the value of the conductivity changes suddenly to a higher value after it was increases linearly, expect

for the MIM-200 nm sample is semiconductor because of the increases indium, a significant increase the number of free electrons turned the material into semiconductors from the beginning. For MIM-50 nm the conductivity changes from  $5.1 \times 10^{-6} (\Omega \text{Cm})^{-1}$  to  $2.7 \times 10^{-5} (\Omega \text{Cm})^{-1}$ , for MIM-75 nm the conductivity is changes from  $5.8 \times 10^{-6} (\Omega \text{Cm})^{-1}$  to  $2.9 \times 10^{-5} (\Omega \text{Cm})^{-1}$ , for MIM-100 nm the conductivity is changes from  $5.0 \times 10^{-6} (\Omega \text{Cm})^{-1}$  to  $2.3 \times 10^{-5} (\Omega \text{Cm})^{-1}$ . The samples become insulator at temperature range from 301 K to 352 K, but becomes semiconductor at temperature range from 379 K to 445 K.

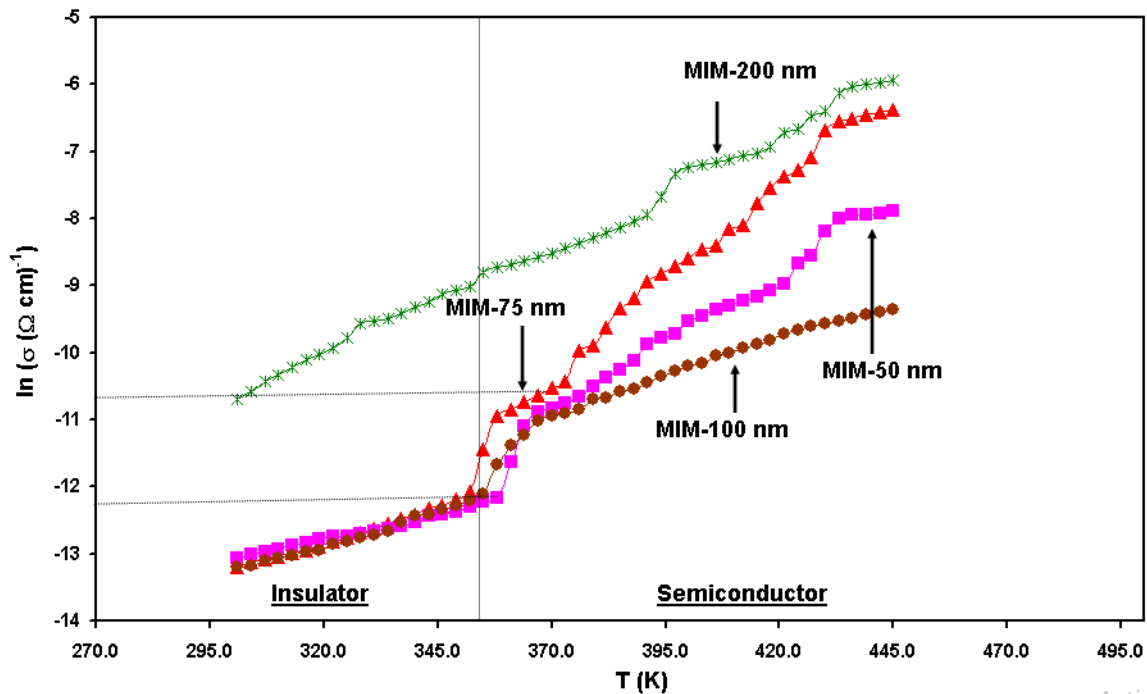


Figure 4.7. Conductivity of Hall bar for all samples  $\ln(\delta)$  Vs  $T$  (K).

By using the data of figure 4.8 and equation (2.21) the activation energy can be calculated. As shown in figure 4.8 there are two linear different regions for the samples MIM- 50, 75,

100, 200 nm, so this data can be used to calculate the activation energy by fitting the data with equation (2.21). Table 4.5 shows the calculated activation energy for the samples.

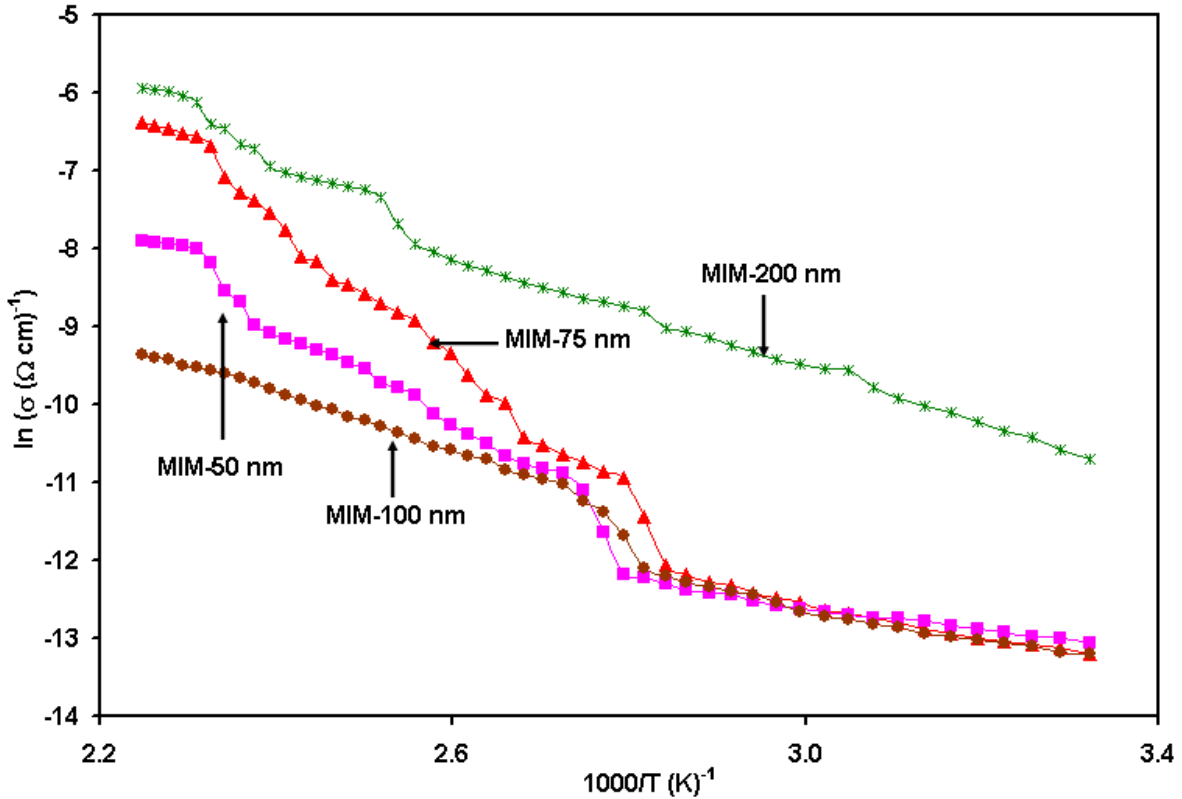


Figure 4.8. Conductivity of Hall bar for all samples  $\ln(\delta)$  Vs  $1000/T (\text{K})^{-1}$ .

The resulting value of the activation energy in table 4.5 had shown a deep donor level for MIM-50 nm which increased when MIM-75 nm. However, it returned to decrease for MIM-100 nm and it returned to increase for MIM-200 nm. The analysis of the conductivity data point out that the current transport mechanism is the thermionic emission of electrons over the potential barrier of semiconductor into the metal. In addition, the activation energy found to be greater than  $kT$ , so it was agreed with the thermionic emission assumption [62].

Moreover, figure 4.9 shown the activation energy versus temperature and displayed a constant variation with temperature, so the thermionic emission theory is valid.

Table 4.5. The activation energy for samples.

Thickness	Ea (HB) <sub>at low temp</sub>	Ea (HB) <sub>at high temp</sub>
MIM-50 nm	193.7	585.8
MIM-75 nm	327.4	788.0
MIM-100 nm	230.9	335.4
MIM-200 nm	378.3	378.3

The activation energy founded by  $\frac{Ln(\delta_2) - Ln(\delta_1)}{\frac{1}{T_2} - \frac{1}{T_1}}$ . Figure 4.9 shows the activation energy Vs temperature which is constant variation with temperature, the activation energy is constant and doesn't change, this means that the current conduction mechanisms are thermionic emission of charge carriers over grain boundaries in crystalline samples (MIM-200 nm) [62], The amorphous samples (MIM-50 nm) appears also to be a thermally excited [63]

The conductivity type is n-type of all sample as it is tested by the "hot-probe" technique.

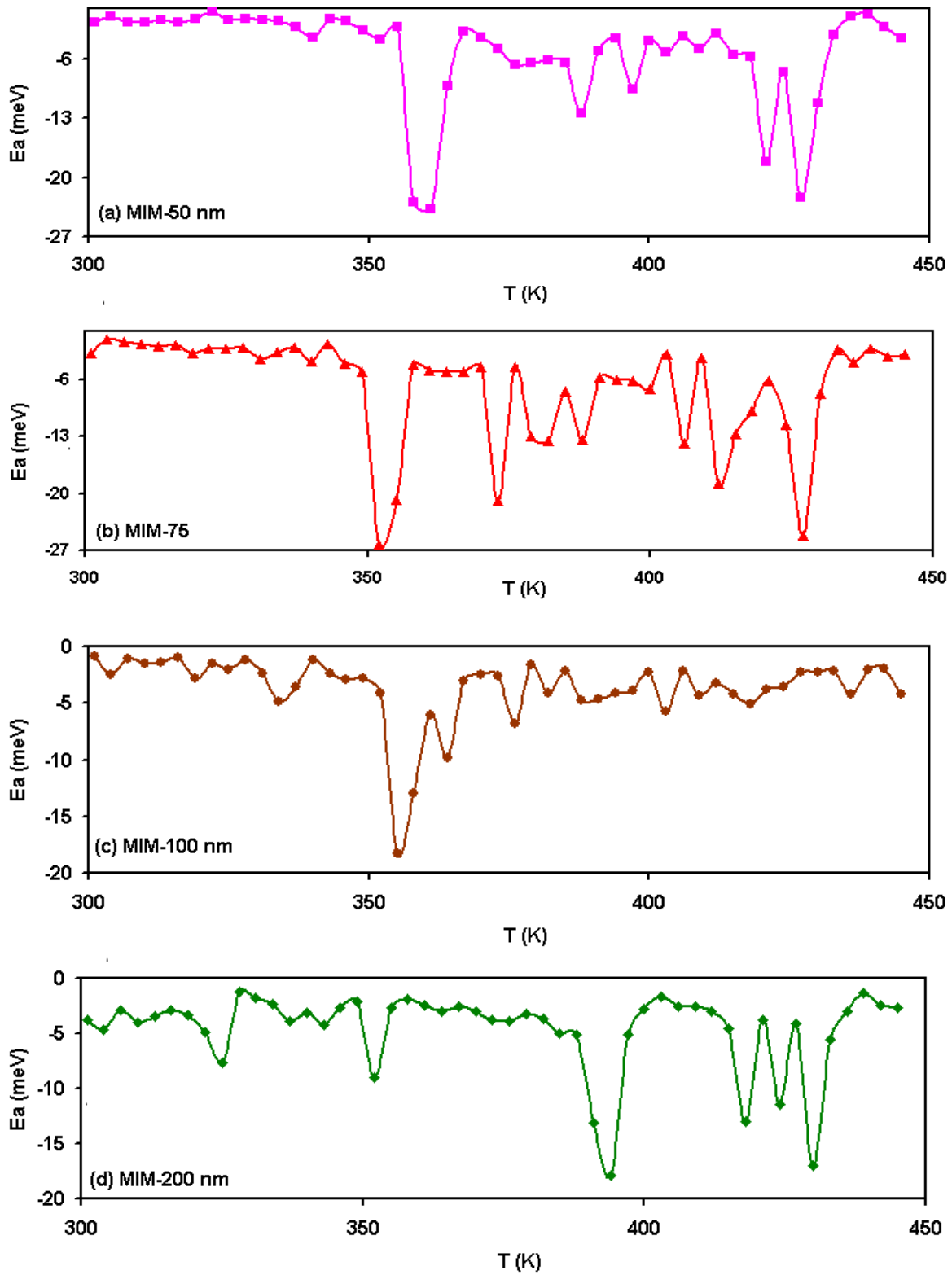


Figure 4.9. Activation energy of Hall bar for all samples.

### 4.3 Impedance Spectroscopy.

In this section the design and characterization of Au/MIM/C passive mode thin film are presented.

Figure 4.10 shows the capacitance spectra of Au/MIM/C films with 0, 50, 75, 100 nm and 200 nm of indium thickness. As observed from the figure of capacitance spectra, there is resonance (series) and anti-resonance (parallel) behavior for all samples except 100 nm thickness. For Au/MIM-0 nm/C, The resonance frequency occurs at  $f_s = 0.28$  GHz while the anti-resonance (negative capacitance) occurs at  $f_p = 0.32$  GHz. In addition, the resonance frequency appeared at 1.7, 0.78, 0.99 GHz and anti-resonance frequency appeared at 1.8, 0.82, 1 GHz, for Au/MIM-50, 75, 200 nm/C, respectively.

To explain the negative capacitance resulting from insertion of minority carriers (tunneling) at forward bias. This property is used to the repeal of positive capacitance in change the signal characteristic of resonant electronic circuits.

Particularly, in time-instituted sensor interfaces to lead the oscillation with enhanced tuning and to raise the tuning scope of voltage controlled oscillators (VCOs) with minimal power impact or phase noise [64-66].

The reasons for the view of the negative capacitances was clarified by the non-equilibrium interfacial states which compel electron conduction by hopping from interfacial to the bulk states, and the minimum significance of the capacitance it referred to the presence of the deep and shallow trap states at the two interfaces [67].

The apparent resonance peaks could be explain by the dynamics of electric dipole, of electrical dipoles. Dipoles are oriented with the external oscillating electric field in a short period of time growing with rising Ac signal frequency. As a consequence, the dielectric constant increases and the number of free charges obtainable for conduction decreases. The increase in dielectric constant cause it an increase in the electric flux density because it reflects the range to which the material focuses electrostatic lines of flux. This operation maintains until the time needed for the dipole guidance is equal to the AC signal time, where the maximum resonance peak appears. For shorter AC signal times (bigger frequency values), the directed dipole with signal is minimum and the dielectric constant lowers. This operation continues until the dipole do not sense the modification of used oscillating electric field, which means access a fixed dielectric constant and thus fixed capacitance [68].

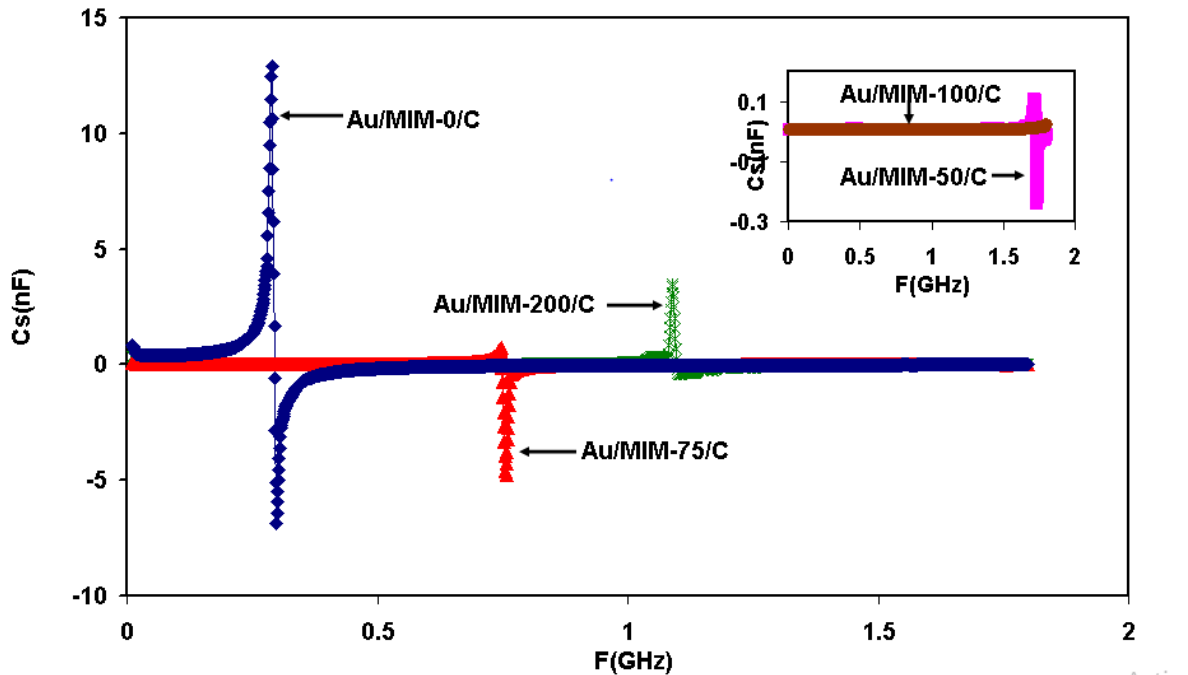


Figure 4.10: The results of the AC signal analysis for the capacitance of Au/MIM/C in the frequency range of 0.01 GHz -1.8 GHz.

The capacitance measured data shown in figure 4.11 is modeled with equation (2.42) to calculate the fitting parameters as shown in table 4.6.

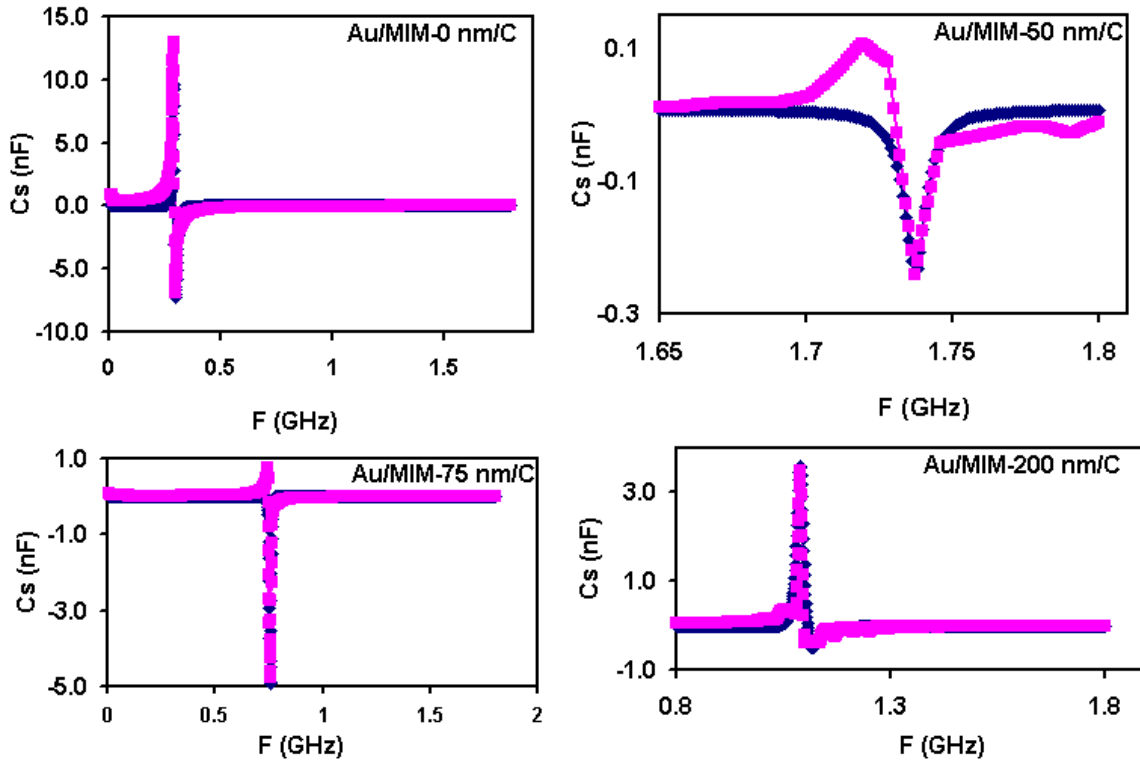


Figure 4.11: The capacitance spectra for the Au/MIM-0, 50, 75, 200 nm/C devices, where the pink line is the experiment data and the blue the modeling data using Equ. (2.29).

In table 4.6 shows fitting parameter of capacitance model. We observed  $\tau_n$  and  $\tau_p$  its decreases by increasing the thickness of indium, but we observed that  $W_n$  and  $W_p$  have the same behavior, they increases by increasing the thickness of indium.

The solution shown in equation (2.42) is also similar to the Drude Lorentz approach for the improvement of the dielectric function assuming linear oscillator slimited by charge carrier-

plasmon coupling and electronic friction terms [69]. This comparison submit that the parameters  $an$  and  $ap$  must be proportional to the free electron and hole densities in the n and p-regions, respectively. Physically, the model can be illustrated as follows. The capacitance is directly proportional to the dielectric constant. The dielectric constant represents the degree of polarization. When an alternating electric field is applied to the material, the electric dipoles oscillate in response to that field. When the frequency of the dipoles is greater than the AC signal frequency, the dielectric constant is constant and no capacitance change can be noticed. As the dipole frequency becomes nearby to signal frequency, all dipoles begin replying to the alternating current signal. The capacitance reaches very high values when signal frequency ( $\omega$ ) equals that of the material's dipole frequency ( $\omega_n$  or  $\omega_p$ ); all dipoles oscillate with the field and no free charge can be observed. When the value of ( $\omega$ ) becomes much greater than that of the dipole, the dielectric constant (capacitance) decreases to a constant frequency independent value. This phenomenon is recognized as a typical resonance phenomenon [70].

Table 4.6: The fitting parameter of capacitance model for Au/MIM/C samples.

	Au/MIM-0 nm/C	Au/MIM-50 nm/C	Au/MIM-75 nm/C	Au/MIM-200 nm/C
$\tau_n$	$2 \times 10^{-8}$	$1.6 \times 10^{-8}$	$1.8 \times 10^{-9}$	$2.5 \times 10^{-10}$
$\tau_p$	$2.3 \times 10^{-8}$	$1.4 \times 10^{-8}$	$9.3 \times 10^{-9}$	$6.6 \times 10^{-10}$
$\omega_n = \omega_p$	$2 \times 10^9$	$1.5 \times 10^{10}$	$2.5 \times 10^{10}$	$3.8 \times 10^{10}$

It is clear from Fig 4.12 that the conductance spectra exhibit a shift in the maximum peak position toward higher frequency values. Particularly, which the maximum appears at 0.311 GHz in the MIM-0 nm sample it appears at 0.749 GHz for the MIM-75 nm and at 1.009 GHz for the MIM-200 nm sample. The shift of the maximum toward the higher frequency could be assigned to the free carrier density which increase with increasing indium thicknesses. The maximum appears at frequencies equivalent to the plasma frequency. The plasma frequency is directly proportional with free carrier density.

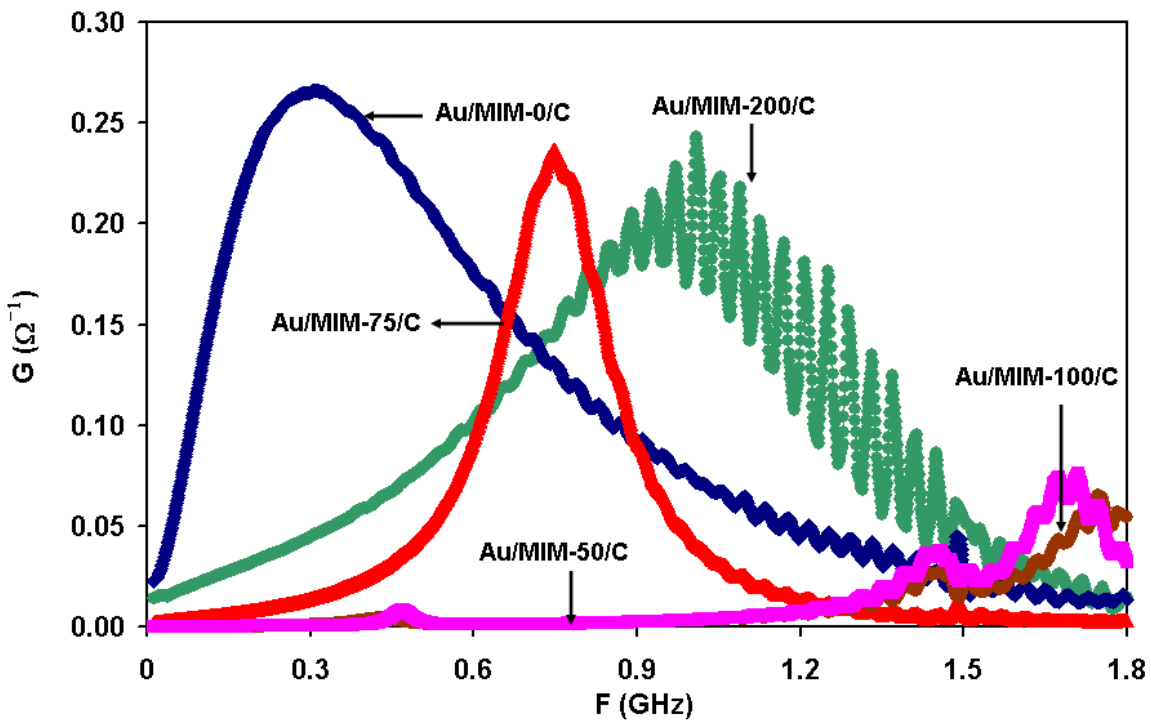


Fig. 4.12: The conductance spectra in the frequency range of (0.01 GHz -1.8 GHz) for Au/MIM-0nm/C, Au/MIM-50nm/C, Au/MIM-75nm/C, Au/MIM-100nm/C, Au/MIM-200nm/C sandwiched films.

Figure 4.13 displays the impedance ( $Z$ ) with frequency for Au/MIM/C samples. The total impact of the AC signal difference are also noted from the impedance spectra which displayed in figure 4.13. For Au / MIM-0 nm / C, Au / MIM- 75 nm / C and Au / MIM-200 nm / C samples, the impedance decreases when frequency increases. For Au/MIM-50 nm/C and Au/MIM-100 nm/C increases reaching at  $90.9 \Omega$  at 0.46 GHz, reach to  $90.3 \Omega$  at 0.36 GHz. It is an advantage of the band stop filters. To detect the high pass / low pass filtering feature of the apparatus, the absolute values of the reflection coefficient spectra in equation (2.43) are found and shown in figure 4.14. The rate  $\rho$  display the quality of the impedance match between the device and source. The figure shows a good match between the device and source at a critical frequency value of 0.47 GHz for Au/MIM-50nm/C in frequency range from 0.4 to 0.54 GHz, at 0.40 GHz for Au/MIM-100nm/C frequency range from 0.24 to 0.5 GHz, and at 1.4 GHz for Au/MIM-75nm/C frequency range from 1.4 to 1.5 GHz. The device appears as low pass band filter. The frequency range from 1.43 to 1.8 Ghz, the device displays high passes filter features [71]. Thus, the critical frequency being 1.45 GHz represents the notch frequency where microwaves are dramatically trapped [72].

The frequency regions where the magnitude of  $\rho$  in Au/MIM-0nm/C and Au/MIM-200nm/C devices decreases pass band filter features appears. The increase in the frequency, is accompanied with the decrease the value of  $\rho$ . The value of  $\rho$  reaches 0.13 at 1.8GHz.

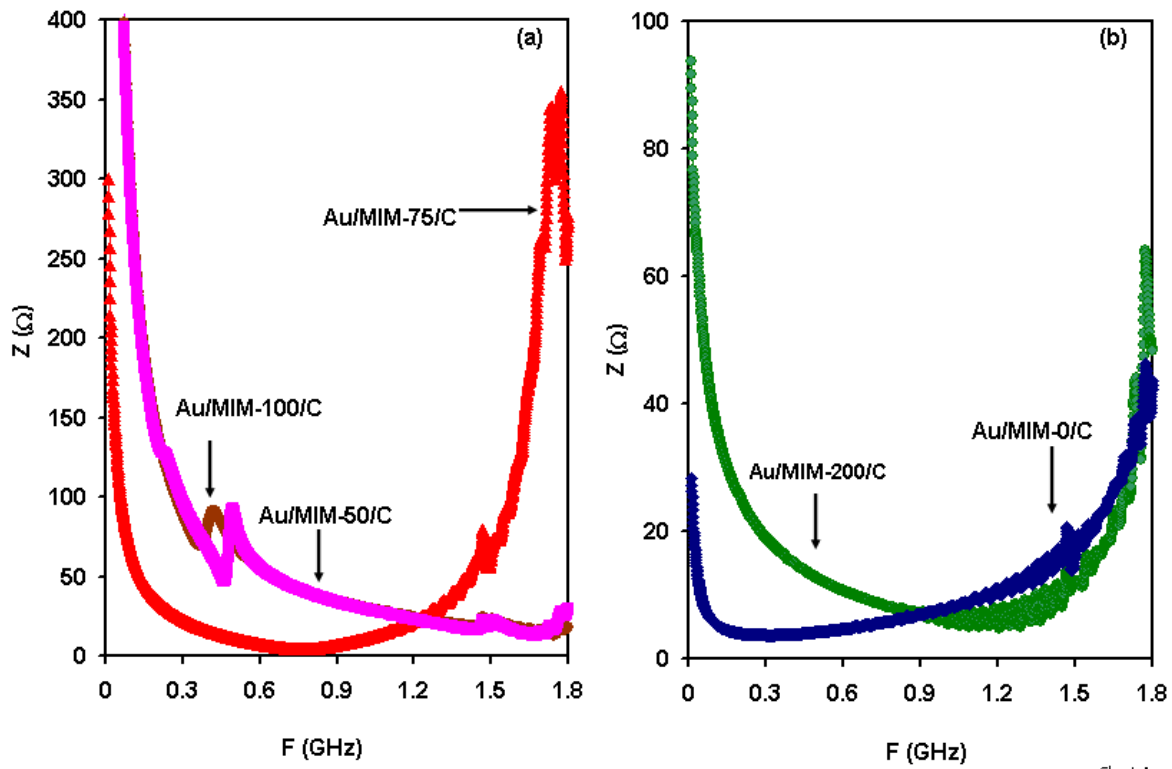


Figure 4.13. The impedance spectral for Au/MIM/C with frequency from zero to 1.8 GHz.

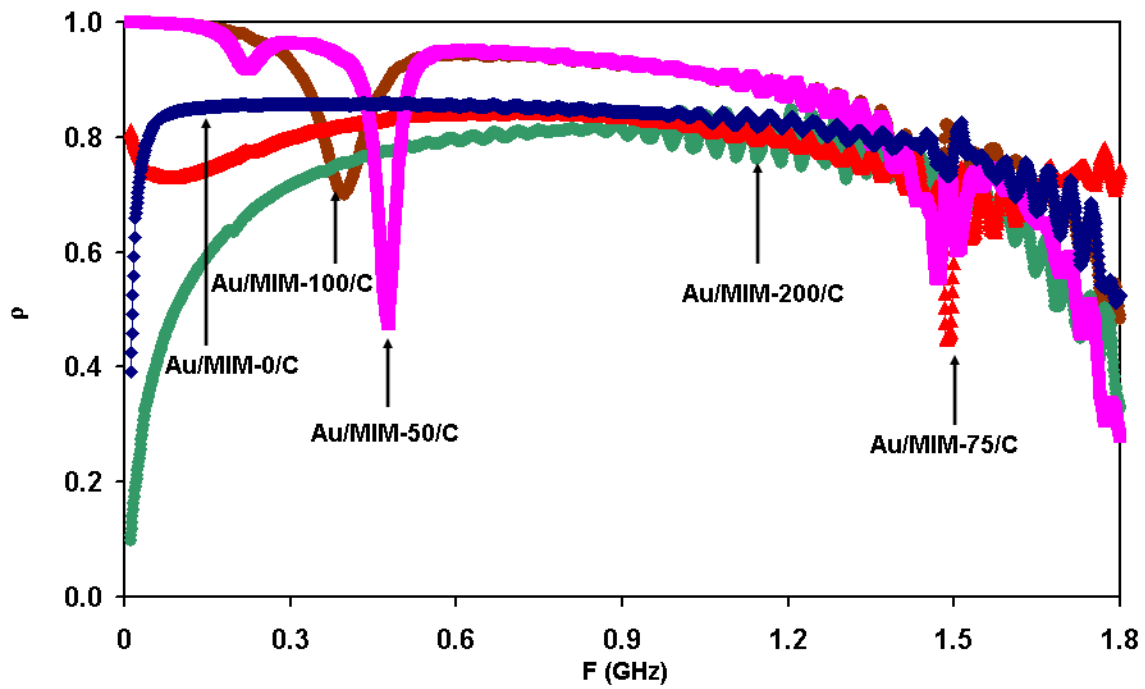


Figure 4.14. The reflection coefficient for Au/MIM/C with frequency from zero to 1.8 GHz.

To detect information about the trap wave quality. On the other hand, the return loss  $L_r$  spectra are found using equation (2.44) and shown in figure 4.15. The increase in the return loss value (ideally must = 20dB), the further qualitative the wave trap. The explained spectra of  $L_r$  submit that Au/MIM-50nm/C, Au/MIM-75nm/C, Au/MIM-100nm/C produce an ideal it's for wave trapping at notch frequency values of 0.47 GHz, 1.49 GHz, 0.4 GHz respectively [73].

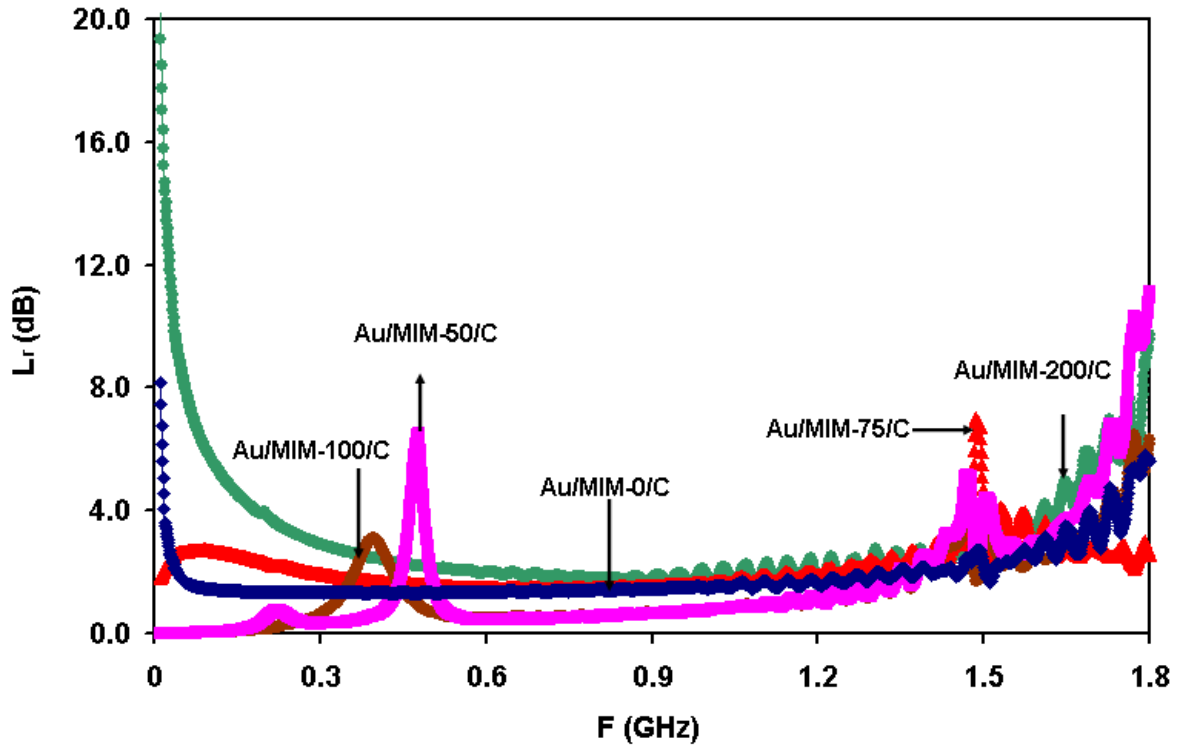


Figure 4.15: The return loss for the Au/MIM/C as a function of frequency in the range of 1.0 MHz-1.8 GHz.

## Chapter Five

### Conclusions

In this thesis,  $\text{MoO}_3$  thin films of thickness of 500 nm were prepared by the thermal evaporation technique through employing physical vapor deposition procedure under vacuum pressure of  $10^{-5}$  mbar. The produced films are used as substrates for the evaporation of indium slabs of thicknesses 0, 50, 75, 100 and 200 nm.

The resulting  $\text{MoO}_3/\text{In}$  films is used as substrate to evaporate another 500 nm thick to  $\text{MoO}_3$  form  $\text{MoO}_3/\text{In}/\text{MoO}_3$  films. The produced films were subjected to X-ray diffraction analysis, temperature dependent conductivity and impedance spectroscopy analysis to research the structural, electrical and impedance characteristics of the films.

The X-ray diffraction analysis has shown that while un-sandwiched and films sandwiched with 50 nm indium layer exhibit amorphous nature of structure, the other samples are weakly polycrystalline. The dominate phase of  $\text{MoO}_3$  is orthorhombic  $\alpha$ -phase. The more thick the indium layer the more intensive the x-ray patterns of tetragonal indium.

The electrical execution of the indium sandwiched films was also scrutinized. The films exhibits an Ohmic nature of contact when it was connect with indium from the top surfaces of the films. Realization of the electrical conductivity of the films was achieved using Hall-bar and Van der Pauw geometry. In the temperature dependent conductivity studies, the conductivity increased with increasing temperature responding to Arrhenius equation. The calculated activation energies of the films increased with increasing the thickness of the indium sandwich.

On the other hand the ac conduction studies have shown that the  $\text{MoO}_3/\text{In}/\text{MoO}_3$  thin film devices are appropriate for AC signal processing. This note was proved with the impedance spectroscopy which appear the possibility of employing these thin film transistors for wave trapping and for application where parasitic repeal of capacitance is necessary. The device actualize this repeal through the negative capacitance character which display in its natural accomplishment.

## References

- [1] Cuando-Espitia, N., Redenius, J., Mensink, K., Camacho-López, M., Camacho-López, S. and Aguilar, G., 2018. Influence of oxygen pressure on the fs laser-induced oxidation of molybdenum thin films. *Optical Materials Express*, 8(3), pp.581-596.
- [2] Zhou, E., Wang, C., Zhao, Q., Li, Z., Shao, M., Deng, X., ... & Xu, X. (2016). Facile synthesis of MoO<sub>2</sub> nanoparticles as high performance supercapacitor electrodes and photocatalysts. *Ceramics International*, 42(2), 2198-2203.
- [3] Sahiner, N. and Demirci, S., 2016. In situ preparation of polyaniline within neutral, anionic, and cationic superporous cryogel networks as conductive, semi-interpenetrating polymer network cryogel composite systems. *Journal of Applied Polymer Science*, 133(46).
- [4] Champsaur, A. M., Hochuli, T. J., Paley, D. W., Nuckolls, C., & Steigerwald, M. L. (2018). Superatom Fusion and the Nature of Quantum Confinement. *Nano letters*.
- [5] Al Orabi, R. A. R., Boucher, B., Fontaine, B., Gall, P., Candolfi, C., Lenoir, B., ... & Gautier, R. (2017). Towards the prediction of the transport properties of cluster-based molybdenum chalcogenides. *Journal of Materials Chemistry C*, 5(46), 12097-12104.
- [6] Zhang, Y., Lin, B., Wang, J., Han, P., Xu, T., Sun, Y., ... & Yang, H. (2016). Polyoxometalates@ Metal-Organic Frameworks Derived Porous MoO<sub>3</sub>@ CuO as Electrodes for Symmetric All-Solid-State Supercapacitor. *Electrochimica Acta*, 191, 795-804.
- [7] Li, N., Li, Y., Li, W., Ji, S. and Jin, P., 2016. One-step hydrothermal synthesis of TiO<sub>2</sub>@ MoO<sub>3</sub> core-shell nanomaterial: microstructure, growth mechanism, and improved photochromic property. *The Journal of Physical Chemistry C*, 120(6), pp.3341-3349.
- [8] Inzani, K., Nematollahi, M., Vullum-Bruer, F., Grande, T., Reenaas, T.W. and Selbach, S.M., 2017. Electronic properties of reduced molybdenum oxides. *Physical Chemistry Chemical Physics*, 19(13), pp.9232-9245.
- [9] Tamboli, P. S., Jagtap, C. V., Kadam, V. S., Ingle, R. V., Vhatkar, R. S., Mahajan, S. S., & Pathan, H. M. (2018). Spray pyrolytic deposition of  $\alpha$ -MoO<sub>3</sub> film and its use in dye-sensitized solar cell. *Applied Physics A*, 124(4), 339.

- [10] Khalate, S. A., Kate, R. S., Pathan, H. M., & Deokate, R. J. (2017). Structural and electrochemical properties of spray deposited molybdenum trioxide ( $\alpha$ -MoO<sub>3</sub>) thin films. *Journal of Solid State Electrochemistry*, 21(9), 2737-2746.
- [11] Ali, F., Khoshsirat, N., Duffin, J. L., Wang, H., Ostrikov, K., Bell, J. M., & Tesfamichael, T. (2017). Prospects of e-beam evaporated molybdenum oxide as a hole transport layer for perovskite solar cells. *Journal of Applied Physics*, 122(12), 123105.
- [12] Kim, Y., Bark, H., Ryu, G.H., Lee, Z. and Lee, C., 2016. Wafer-scale monolayer MoS<sub>2</sub> grown by chemical vapor deposition using a reaction of MoO<sub>3</sub> and H<sub>2</sub>S. *Journal of Physics: Condensed Matter*, 28(18), p.184002.
- [13] Chithambararaj, A., Rajeswari Yogamalar, N. and Bose, A.C., 2016. Hydrothermally synthesized h-MoO<sub>3</sub> and  $\alpha$ -MoO<sub>3</sub> nanocrystals: new findings on crystal-structure-dependent charge transport. *Crystal Growth & Design*, 16(4), pp.1984-1995.
- [14] Domínguez, A., Dutt, A., de Melo, O., Huerta, L., & Santana, G. (2018). Molybdenum oxide 2-D flakes: role of thickness and annealing treatment on the optoelectronic properties of the material. *Journal of Materials Science*, 53(8), 6147-6156.
- [15] Lin, Shih-Yuan, et al. "Electrochromic properties of MoO<sub>3</sub> thin films derived by a sol-gel process." *Journal of sol-gel science and technology* 53.1 (2010): 51-58.
- [16] Kamoun, O., Boukhachem, A., Amlouk, M. and Ammar, S., 2016. Physical study of Eu doped MoO<sub>3</sub> thin films. *Journal of Alloys and Compounds*, 687, pp.595-603.
- [17] Kariper, İ.A. and Tezel, F.M., 2018. Producing MoO<sub>3</sub> Thin film Supercapacitor through Bio-chemical Bath Deposition. *Ceramics International*.
- [18] Molina-Mendoza, A.J., Lado, J.L., Island, J.O., Niño, M.A., Aballe, L., Foerster, M., Bruno, F.Y., López-Moreno, A., Vaquero-Garzon, L., van der Zant, H.S. and Rubio-Bollinger, G., 2016. Centimeter-scale synthesis of ultrathin layered MoO<sub>3</sub> by van der Waals epitaxy. *Chemistry of Materials*, 28(11), pp.4042-4051.
- [19] Inzani, K., Grande, T., Vullum-Bruer, F. and Selbach, S.M., 2016. A van der Waals density functional study of MoO<sub>3</sub> and its oxygen vacancies. *The Journal of Physical Chemistry C*, 120(16), pp.8959-8968.
- [20] Badr, A.M., El-Anssary, E.H., Elshaikh, H.A. and Afify, H.H., 2017. Hydrothermal synthesis and influence of later heat treatment on the structural evolution, optical and

electrical properties of nanostructured  $\alpha$ -MoO<sub>3</sub> single crystals. *Journal of Physics D: Applied Physics*, 50(50), p.505111.

[21] Yang, C.S., Shang, D.S., Chai, Y.S., Yan, L.Q., Shen, B.G. and Sun, Y., 2016. Moisture effects on the electrochemical reaction and resistance switching at Ag/molybdenum oxide interfaces. *Physical Chemistry Chemical Physics*, 18(18), pp.12466-12475.

[22] Magini, M., 2018. *X-Ray Diffraction of Ions in Aqueous Solutions: Hydration and Complex Formation: 0*. CRC press.

[23] Hughes, L., 2018. Bragg's Law and Diffraction. *Bulletin of the American Physical Society*, 63.

[24] Franco, M.K.K.D., de Araújo, D.R., de Paula, E., Cavalcanti, L. and Yokaichiya, F., 2017. X-Ray Scattering Techniques Applied in the Development of Drug Delivery Systems. In *X-ray Scattering*. InTech.

[25] Waeselmann, N., 2012. Structural transformations in complex perovskite-type relaxor and relaxor-based ferroelectrics at high pressures and temperatures.

[26] Dinnebier, Robert E., and Simon JL Billinge, eds. Powder diffraction: theory and practice. Royal Society of Chemistry, 2008.

[27] M. Dressel and G. Gruner, *Electrodynamics of solids: optical properties of electrons in matter*, Cambridge Press, 2003, pp. 34-97.

[28] Nong, H. T. T., et al. "Stacking faults density driven collapse of magnetic energy in hcp-cobalt nano-magnets." *Advances in Natural Sciences: Nanoscience and Nanotechnology* 8.2 (2017): 025012.

[29] Sze, Simon M., and Kwok K. Ng. *Physics of semiconductor devices*. John wiley & sons, 2006.

[30] S. Laszlo and D. Walsh, *Electrical properties of materials*, OUP Oxford, 2009, pp. 1-121.

[31] Y. Zhang, M. Wang, Z. Le, G. Huang, L. Zou and Z. Chen, "Preperation and Characterization of pyrochlore oxide Y<sub>2</sub>Ti<sub>2</sub>O<sub>7</sub> nanocrystals via gel-combustion route," *Ceramics International*, vol. 40, no. 4, pp. 5223-5230, 2014.

- [32] Hmurcik, L.V., Patel, S. and Gupta, N., 2018. On the Use of van der Pauw Technique to Monitor Skin Burning in Patients Undergoing Interferential Current Therapy (IFC) with Extension to Other E-Stim Monitoring. In *Information Technology-New Generations* (pp. 659-664). Springer, Cham.
- [33] Pues, Hugo F., and Antoine R. Van De Capelle. "An impedance-matching technique for increasing the bandwidth of microstrip antennas." *IEEE transactions on antennas and propagation* 37.11 (1989): 1345-1354.
- [34] Khusayfan, N.M., Qasrawi, A.F. and Khanfar, H.K., 2018. Design and electrical performance of CdS/Sb<sub>2</sub>Te<sub>3</sub> tunneling heterojunction devices. *Materials Research Express*, 5(2), p.026303.
- [35] Ershov, Maxim, et al. "Negative capacitance effect in semiconductor devices." *IEEE Transactions on Electron Devices* 45.10 (1998): 2196-2206.
- [36] Khusayfan, Najla M., A. F. Qasrawi, and Hazem Khanfar. "Design and electrical performance of CdS/Sb<sub>2</sub>Te<sub>3</sub> tunneling heterojunction devices." *Materials Research Express* (2018).
- [37] Bakshi, U. A., and A. V. Bakshi. *Network analysis*. Technical Publications, 2009.
- [38] Macnamara, Thereza. *Introduction to antenna placement and installation*. John Wiley & Sons, 2010.
- [39] Shaheen, R. and Bashir, J., 2010. Ca<sub>2</sub>CoNbO<sub>6</sub>: A new monoclinically distorted double perovskite. *Solid State Sciences*, 12(8), pp.1496-1499.
- [40] Wilson, Adam A., et al. "Thermal conductivity measurements of high and low thermal conductivity films using a scanning hot probe method in the 3  $\omega$  mode and novel calibration strategies." *Nanoscale* 7.37 (2015): 15404- 15412.
- [41] Araki, Takeshi, et al. "High critical current density scheme of YBa<sub>2</sub>Cu<sub>3</sub>O<sub>7-x</sub> films by the metalorganic deposition using trifluoroacetates." *Superconductor Science and Technology* 15.6 (2002): 913.
- [42] Jeong, Jaewoo, et al. "Suppression of metal-insulator transition in VO<sub>2</sub> by electric field-induced oxygen vacancy formation." *Science* 339.6126 (2013): 1402-1405.
- [43] Tojo, T., Tawa, H., Oshida, N., Inada, R. and Sakurai, Y., 2018. Electrochemical characterization of a layered  $\alpha$ -MoO<sub>3</sub> as a new cathode material for calcium ion batteries. *Journal of Electroanalytical Chemistry*, 825, pp.51-56.

- [44] Omareya, O.A., Qasrawi, A.F. and Al Garni, S.E., 2017. Effect of Au nanosandwiching on the structural, optical and dielectric properties of the as grown and annealed InSe thin films. *Physica B: Condensed Matter*, 520, pp.57-64.
- [45] Al Garni, S.E., Omareye, O.A. and Qasrawi, A.F., 2017. Growth and characterization of InSe/Ge/InSe interfaces. *Optik-International Journal for Light and Electron Optics*, 144, pp.340-347.
- [46] Zhao, B., Zhang, L., Zhen, D., Yoo, S., Ding, Y., Chen, D., Chen, Y., Zhang, Q., Doyle, B., Xiong, X. and Liu, M., 2017. A tailored double perovskite nanofiber catalyst enables ultrafast oxygen evolution. *Nature communications*, 8, p.14586.
- [47] Lee, W.C., Tan, L.L., Sumathi, S. and Chai, S.P., 2018. Copper-doped flower-like molybdenum disulfide/bismuth sulfide photocatalysts for enhanced solar water splitting. *International Journal of Hydrogen Energy*, 43(2), pp.748-756.
- [48] Trukhanov, S.V., Trukhanov, A.V., Turchenko, V.A., Trukhanov, A.V., Trukhanova, E.L., Tishkevich, D.I., Ivanov, V.M., Zubar, T.I., Salem, M., Kostishyn, V.G. and Panina, L.V., 2018. Polarization origin and iron positions in indium doped barium hexaferrites. *Ceramics International*, 44(1), pp.290-300.
- [49] Pan, Y., Wang, S., Mao, P. and Jin, C., 2017. Role of Si concentration on the thermodynamic properties of molybdenum silicides. *Vacuum*, 141, pp.170-172.
- [50] Kubota, Y., Dy, E.S., Nakanishi, H., Kasai, H. and Diño, W.A., 2006. A first principles investigation on the interaction of oxomolybdenum porphyrin with O<sub>2</sub>—Oxomolybdenum porphyrin as a catalyst for oxygen reduction—. *e-Journal of Surface Science and Nanotechnology*, 4, pp.630-635.
- [51] Gurlo, A., Barsan, N., Ivanovskaya, M., Weimar, U. and Göpel, W., 1998. In<sub>2</sub>O<sub>3</sub> and MoO<sub>3</sub>–In<sub>2</sub>O<sub>3</sub> thin film semiconductor sensors: interaction with NO<sub>2</sub> and O<sub>3</sub>. *Sensors and Actuators B: Chemical*, 47(1-3), pp.92-99.
- [52] Wang, C., Wang, H.I., Tang, W.T., Luo, C.W., Kobayashi, T. and Leu, J., 2011. Superior local conductivity in self-organized nanodots on indium-tin-oxide films induced by femtosecond laser pulses. *Optics express*, 19(24), pp.24286-24297.
- [53] Moreno, O. Portillo, R. Gutiérrez Pérez, R. Palomino Merino, M. Chávez Portillo, MN Márquez Specia, ME Hernández Torres, M. Gracia Jiménez, J. R. Cerna, and M. Zamora Tototzintle. "Near-infrared-to-visible upconverting luminescence of Er<sup>3+</sup>-doped CdS nanocrystals grown by chemical bath." *Optik-International Journal for Light and Electron Optics* 138 (2017): 229-239.

- [54] Ahamad, Tansir, MA Majeed Khan, Sushil Kumar, Maqsood Ahamed, Mohammed Shahabuddin, and Abdulaziz N. Alhazaa. "CdS quantum dots: growth, microstructural, optical and electrical characteristics." *Applied Physics B* 122, no. 6 (2016): 1-8.
- [55] Rellán-Piñero, M. and Lopez, N., 2018. One Oxygen Vacancy, Two Charge States: Characterization of Reduced  $\alpha$ -MoO<sub>3</sub> (010) through Theoretical Methods. *The journal of physical chemistry letters*.
- [56] Noh, H.J., Kim, J.W., Lee, S.M. and Jang, H., 2017. Effect of grain size on the electrical failure of copper contacts in fretting motion. *Tribology International*, 111, pp.39-45.
- [57] Qasrawi, A. F., Ziqan, A. M., Jazzar, S. K., & Gasanly, N. M. (2015). Photon assisted hopping conduction mechanism in Tl<sub>2</sub>SSe crystals. *Physica B: Condensed Matter*, 458, 149-154.
- [58] Smyth, R.T., Johnson, C.A., Ennis, D.A., Loch, S.D., Ramsbottom, C.A. and Ballance, C.P., 2017. Relativistic R-matrix calculations for the electron-impact excitation of neutral molybdenum. *Physical Review A*, 96(4), p.042713.
- [59] Walsh, A., Sokol, A.A., Buckeridge, J., Scanlon, D.O. and Catlow, C.R.A., 2017. Electron counting in solids: oxidation states, partial charges and ionicity. *arXiv preprint arXiv:1704.05140*.
- [60] Ayadi, T., Debbichi, L., Said, M. and Lebègue, S., 2017. An ab initio study of the electronic structure of indium and gallium chalcogenide bilayers. *The Journal of Chemical Physics*, 147(11), p.114701.
- [61] Jadhao, V. and Robbins, M.O., 2017. Reply to Bair: Crossover to Arrhenius behavior at high viscosities in squalane. *Proceedings of the National Academy of Sciences*, 114(42), pp.E8807-E8808.
- [62] Navarro, D., Herrera, F., Zenitani, H., Miura-Mattausch, M., Yorino, N., Mattausch, H.J., Takusagawa, M., Kobayashi, J. and Hara, M., 2018. Compact modeling of SiC Schottky barrier diode and its extension to junction barrier Schottky diode. *Japanese Journal of Applied Physics*, 57(4S), p.04FR03.
- [63] Sun, C., Wang, M.S., Li, P.X. and Guo, G.C., 2017. Conductance Switch of a Bromoplumbate Bistable Semiconductor by Electron-Transfer Thermochromism. *Angewandte Chemie International Edition*, 56(2), pp.554-558.
- [64] Qasrawi, A. F. "Fabrication of Al/MgO/C and C/MgO/InSe/C tunneling barriers for tunable negative resistance and negative capacitance applications." *Materials Science and Engineering: B* 178.12 (2013): 851-856.

- [65] Wu, Qiyang, et al. "Frequency tuning range extension in LC-VCOs using negative capacitance circuits." *IEEE Transactions on Circuits and Systems II: Express Briefs* 60.4 (2013): 182-186.
- [66] Kmail, Renal RN, and A. F. Qasrawi. "Physical design and dynamical analysis of resonant–antiresonant Ag/MgO/GaSe/Al optoelectronic microwave devices." *Journal of Electronic Materials* 44.11 (2015): 4191-4198.
- [67] Khusayfan, Najla M., A. F. Qasrawi, and Hazem Khanfar. "Design and electrical performance of CdS/Sb<sub>2</sub>Te<sub>3</sub> tunneling heterojunction devices." *Materials Research Express* (2018).
- [68] Qasrawi, A. F., and N. M. Gasanly. "Investigation of the electrical parameters of Ag/pTlGaSeS/C Schottky contacts." *Materials Science and Engineering: B* 177.12 (2012): 981985.
- [69] Nilsson, P.O., 1970. Electronic structure of disordered alloys: optical and photoemission measurements on Ag-Au and Cu-Au alloys. *Physik der kondensierten Materie*, 11(1), pp.1-18.
- [70] Khusayfan, N.M., Qasrawi, A.F. and Khanfar, H.K., 2018. Design and electrical performance of CdS/Sb<sub>2</sub>Te<sub>3</sub> tunneling heterojunction devices. *Materials Research Express*, 5(2), p.026303.
- [71] Khusayfan, N.M., Qasrawi, A.F. and Khanfar, H.K., 2018. Design and characterization of Au/In<sub>4</sub>Se<sub>3</sub>/Ga<sub>2</sub>S<sub>3</sub>/C field effect transistors. *Results in physics*, 8, pp.1239-1244.
- [72] Pozar Dm. *Microwave Engineering*. India: Wiley ;2015.
- [73] Abed, T.Y., Qasrawi, A.F. and Al Garni, S.E., 2018. Investigation of the physical properties of the Yb nanosandwiched CdS films. *Journal of Alloys and Compounds*, 731, pp.1022-1028.

## تحسين الاداء الكهربائي لمركب المالبوديوم اوكسايد بواسطة شرائح الانديوم النانومترية

### الملخص

قمنا بتحضير عينات المولبوديوم اوكسايد بسمك 500 نم لكل طبقة، في هذه الاطروحة تم تحسين الخصائص الكهربائية لعنصر المولبوديوم اوكسايد وتم تحضير عينة المولبوديوم اوكسايد بطبقتين ، وبعد ذلك تم زراعة عنصر الانديوم بسمك مختلف بين طبقتين المولبوديوم اوكسايد وقمنا بدراسة الخصائص الكهربائية لعنصر المولبوديوم اوكسايد وأخرى عند زراعة الانديوم . وقمنا بحساب الموصلية عند درجة حرارة الجو وبعد ذلك قمنا بتسخين العينات الى درجة حرارة 130 س وقمنا بحساب الموصلية عند درجات حرارة مختلفة . ودراسة تأثير زراعة الانديوم على خصائص المولبوديوم اوكسايد.

وتم أيضا دراسة الخصائص التركيبية لعنصر المولبوديوم اوكسايد والتعرف على التركيب البلوري . ودراسة تأثير زراعة الانديوم على التركيب البلوري له .

وفي النهاية شملت الدراسة خصائص الطيف لهذا العنصر في تردد يصل الى 1.8 جيجا هيرتز. وتبين أن موسعة هذه المادة هي سالبة وأنها تمتلك خاصية حدوث رنين على تردد 0.3 جيجا هيرتز وتزداد هذه الخاصية بزيادة عنصر الانديوم وهذا له استخدامات في التطبيقات التكنولوجية.